AIAA JOURNAL
Vol. 60, No. 8, August 2022

Higher-Order Approximations for Stabilizing Zero-Energy Modes in Non-Ordinary State-Based Peridynamics Models

Iman Javaheri,* Jiangyi Luo,† Aaditya Lakshmanan,‡ and Veera Sundararaghavan§
University of Michigan, Ann Arbor, Michigan 48105

https://doi.org/10.2514/1.J061453

The non-ordinary state-based peridynamics theory combines non-local dynamic techniques with a desirable correspondence material principle, allowing for the use of continuum mechanics constitutive models. Such an approach presents a unique capability for solving problems involving discontinuities (e.g., fracture and crack propagation). However, the correspondence-based peridynamics models often suffer from zero-energy mode instabilities in numerical implementation, primarily due to the weak integral formulation in non-local approximations of the deformation gradient tensor. This paper focuses on a computational scheme for eliminating the zero-energy mode oscillations using a choice of influence functions that improve the truncation error in a higher-order Taylor series expansion of the deformation gradient. The novelty here is a tensor-based derivation of the linear constraint equations, which can be used to systematically identify the particle interaction weight functions for various user-specified horizon radii. In this paper, the higher-order stabilization scheme is demonstrated for multi-dimensional examples involving polycrystalline and composite microstructures, along with comparisons against conventional finite element methods. The proposed stabilization scheme is shown to be highly effective in suppressing the spurious zero-energy mode oscillations in all of the numerical examples.

Nomenclature

$\boldsymbol{b}$	=	body force density
$\boldsymbol{F}$	=	deformation gradient tensor
$\boldsymbol{f}$	=	force vector
h	=	particle spacing for an uniform discretization
$\boldsymbol{K}$	=	symmetric positive-definite shape tensor
N	=	number of material particles within self-centered horizon, $\mathcal{H}_{\boldsymbol{x}}$
$\boldsymbol{P}$	=	first Piola–Kirchoff stress tensor
$\boldsymbol{u}$	=	displacement vector
$\boldsymbol{x}$	=	reference bond vector
Δt	=	incremental time step
δ	=	horizon size
δ_{ij}	=	Kronecker delta
$\delta\boldsymbol{y}$	=	deformed bond vector
$\boldsymbol{\xi}$	=	bond vector
ω	=	weighting coefficients of neighboring particles in self-centered horizon, $\mathcal{H}_{\boldsymbol{x}}$

I. Introduction

MODELING mechanical performance of metallic alloys for aerospace applications remains an ongoing area of research in the material science community [1]. One of the popular numerical techniques for modeling polycrystalline aggregates is the crystal plasticity finite element (CPFE) technique [2,3], which describes dislocation motions and their interactions using continuum mechanics principles. Finite element (FE) modeling of polycrystalline materials using crystal plasticity (CP) theory [4–7] has allowed for a greater understanding of mechanical behavior (e.g., stress and strain response), texture evolution, and crystallographic slip response. Such a capability has led to the development of high-strength aluminum alloys [8,9], soft magnetic materials with low hysteresis [10], and multifunctional alloys with high-field induced strains [11–13]. Nonetheless, the standard FE models often run into difficulties when modeling the local mechanical response of materials in the presence of discontinuities (e.g., voids, cracks, and soft precipitates). The magnitude of mechanical quantities computed by the standard finite element method (FEM) is also highly dependent on the elemental size [1,14], necessitating costly iterative mesh refinement procedures along with considerable experimental efforts for numerical calibration [15,16]. Improvements have been proposed for CPFE models to address the issue of mesh dependency. The extended-FEM (X-FEM) and variational multiscale method (VMM) enrich the computational space by introducing a sharp, discontinuous interpolating function to trigger strain localizations at the crack tip [17]. Nevertheless, these techniques are not capable of predicting small-scale localizations naturally as a consequence of the underlying principles. Thus, imperfections are often imposed to trigger the strain localizations [18]. Alternatively, the mesh-free state-based peridynamics (PD) technique [19–22], which replaces the traditional differential equations with an integral form of the non-local continuum mechanics theory, has attracted significant attention for predicting damage nucleation and propagation with an intrinsic characteristic length scale [18,23–26]. Figure 1 compares the strain fields obtained by crystal plasticity PD (CPPD) and CPFE simulations against reference experimental imaging. While both CPPD and CPFE capture comparable trends in the strain fields, CPPD depicts localized patterns similar to the experiments that are typically shown to be well-resolved, and otherwise smoothed out by CPFE.

In the initial version of the PD as introduced in [19], a bond-based technique was employed in which forces in-between material particles were assumed to be pairwise, i.e., equal and direction-reversed. As a consequence of such an assumption, the bond-based PD method is restricted to fixed values of Poisson's ratio [27,28]. This limits the general applicability of the bond-based PD approach and the possibility

Presented as Paper 2022-0073 at the AIAA SciTech 2022 Forum, San Diego, CA, and Virtual Event, January 3–7, 2022; received 11 November 2021; revision received 6 March 2022; accepted for publication 27 April 2022; published online 31 May 2022.

*Ph.D. Candidate, Department of Aerospace Engineering; also Student Trainee, Durability, Damage Tolerance, and Reliability Branch, NASA Langley Research Center, Hampton, Virginia 23681; imanajv@umich.edu, iman.javaheri@nasa.gov. Student Member AIAA.

†Ph.D. Candidate, Department of Mechanical Engineering; jiangyi@umich.edu.

‡Ph.D. Candidate, Department of Aerospace Engineering; aadityal@umich.edu.

§Professor, Department of Aerospace Engineering; veeras@umich.edu. Member AIAA.

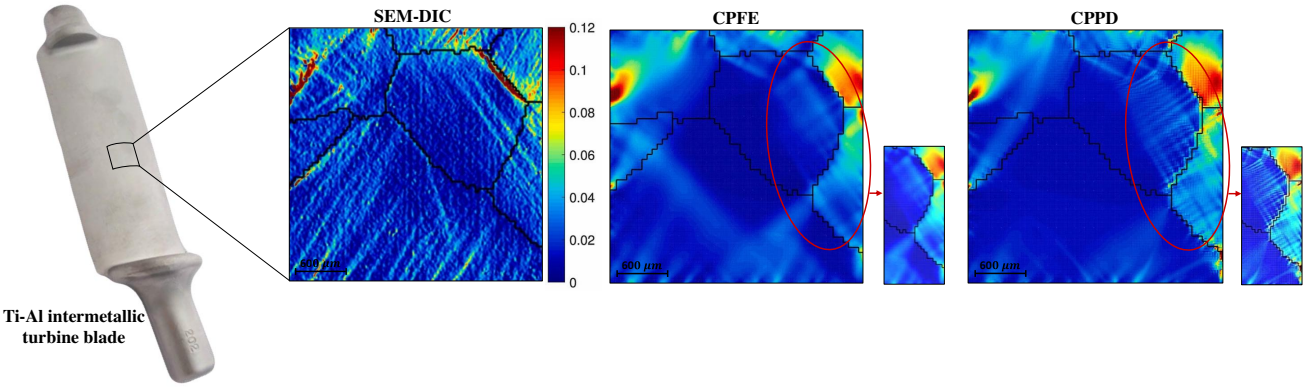

Fig. 1 Experimental instrumentations such as scanning electron microscopy with the combination of digital image correlation (SEM-DIC) have shown that microscale strain localizations on the surface of polycrystalline aggregates can act as precursors for damage nucleation and degradation in material strength [18]. Unlike conventional CPFE models, CPPD models are shown to be capable of predicting such localizations naturally as a consequence of the underlying physics.

for simulations of complex material deformations such as in plasticity [29]. A more comprehensive PD scheme, commonly referred to as the non-ordinary state-based PD, was subsequently proposed in which force states were defined by the interactions between the material particles [27]. This presents a generalized form of the PD, allowing material particles to carry forces in all directions [30]. In this approach, the non-locality is conveniently applied without the need to alter the underlying constitutive principles and failure criteria [21,31]. Accordingly, this paper employs a non-ordinary state-based version of the PD theory to model microstructural domains consisting of material particles (i.e., pixels in 1D/2D and voxels in 3D) with a uniform discretization interacting across a finite horizon radius. The interacting forces in-between the material particles are computed from the stress tensors obtained by the crystal plasticity constitutive model [29]. This approach has been proven to be advantageous for modeling discontinuities as well as microscale localizations when compared to the conventional continuum mechanics models [21,22,32].

A particular drawback of the non-ordinary state-based PD using correspondence material models is the presence of zero-energy (also known as hourglass) instability modes, due to the weak integral formulation in non-local approximations of the deformation gradient tensor [23,33–35]. Such instability modes often worsen with enlarged horizon interactions, interparticle spacing, and regions with high-strain gradients. Recently, different frameworks have been proposed to mitigate the spurious instability oscillations by introducing fictitious bonds between material particles [36–38]. Even though these bond-based techniques provide an artificial stiffness for stability by introducing a supplementary term of various forms to the force vector states, they do not provide resolutions to the fundamental problem. They are also highly sensitive to particle spacing and require additional parameters that need to be calibrated on a case-by-case basis through repetitive numerical simulations [39]. Moreover, to alleviate the zero-energy mode oscillations, Wu and Ben [40] proposed replacement of the displacement components of the center material particles with a weighted average displacement of all neighboring particles in their respective horizon interactions. Although this approach eliminates the need for supplementary fictitious bonds, the issue of zero-energy mode oscillations still appears to remain, particularly in the strain/stress fields. Alternatively, in the work of Luo and Sundararaghavan [41], each finite horizon within a nearest-neighbor PD family is assigned with a stress point at which derivatives of field variables are computed in order to enhance the particle connectivity. Such an approach is further enhanced in Cui et al. [42] by introducing higher-order peridynamic derivatives, incorporating horizon sizes beyond nearest-neighbor interactions. Subsequent improvements are also presented based on higher-order operators to solve the non-local PD equations up to an arbitrary degree of accuracy [43–48]. Although these techniques address the fundamental problem in the correspondence formulation that leads to zero-energy oscillations, they often require extensive computational efforts, reducing the general applicability of such stabilization procedures.

In microstructural simulations, uniform pixel- or voxel-based structured discretizations are conveniently obtained from microscopy and numerical acquisition techniques [3,49,50]. As a result, this paper primarily focuses on developing particle interaction weight functions for uniformly structured grids based on the non-ordinary state-based PD implementation via Newmark's dynamic method with artificial damping [51]. Here, a tensor formulation of the constraint equations on discrete influence weight functions for both 1D and higher-dimensional problems is presented based on Taylor series expansion of the deformation gradient [30]. Four numerical examples are subsequently studied to demonstrate the applicability of the proposed higher-order weight functions for mitigation of the zero-energy mode oscillations. Elasticity problems are tested first in order to understand the numerical behavior of the algorithm comprehensively. The PD solver is compared against the FEM for predicting the stress and strain localization, texture development, and homogenized stress–strain response. The proposed high-order formulation is demonstrated to be effective in suppressing the zero-energy mode oscillations in materials with long-range particle interactions, consisting of both polycrystalline and composite microstructures.

The paper is organized as follows. A review of the non-ordinary state-based PD is first outlined in Sec. II.A. In Sec. II.B, a brief explanation on the origin of zero-energy modes follows. The higher-order approximation theory of deformation gradient is then proposed in Sec. II.C. Numerical examples are shown and discussed in Sec. III for various multi-dimensional problems. Notably, in Sec. III.A, the higher-order approximation results for a number of long-range interactions are compared against the analytical solutions and PD methods without any stabilization control [52] for a simple case of 1D cantilever bar. Effects of zero-energy mode oscillations on 2D polycrystalline microstructures involving texture evolution are then introduced in Sec. III.B. Thereafter, the CPPD numerical results are examined against conventional CPFE techniques in modeling fine length-scale shear bands across polycrystalline aggregates. This follows by Secs. III.C and III.D, which, respectively, demonstrate 3D examples of composite and polycrystalline microstructures subjected to Dirichlet boundary conditions. Here, the proposed PD technique is shown to be superior to CPFE models in simulating the sharp small-scale strain localizations across the microstructural interface.

II. Methodology

In Sec. II.A, the non-local state-based PD theory is briefly reviewed. Thereafter in Sec. II.A.1, the discretization process along with an overview of the numerical implementation of the PD algorithm is outlined. Next in Sec. II.B, the zero-energy mode oscillation and its relationship with the material particle interactions are discussed. In Sec. II.C, a novel solution for suppressing the zero-energy instability noise for 1D, 2D, and 3D problems

using higher-order approximations of deformation gradients is introduced. Next, in Sec. II.D, a boundary treatment based on constant deformation gradient is introduced that encompasses large horizon interactions.

A. Non-Ordinary State-Based Peridynamics

The non-ordinary state-based PD theory forms the foundation of the present work. This model was first proposed by Silling et al. [27] and consists of a non-local integral reformulation of the classical continuum mechanical theory. Unlike bond-based PD models [19,53], which are restricted to a specific Poisson's ratio, the state-based PD theory can be generalized to include various classical constitutive material models, enabling the integration with crystal elastoplasticity [18].

Consider a material particle in the reference configuration at position $\boldsymbol{x}$, which can only interact with its neighboring points in a self-centered horizon $\mathcal{H}_x$, within a finite radius δ. Given the displacement field $\boldsymbol{u}$ of the material particle at $\boldsymbol{x}$, the deformed location of the corresponding material particle in the current configuration is represented as $\boldsymbol{y} = \boldsymbol{x} + \boldsymbol{u}$. Here, as depicted in Fig. 2, the reference configuration of the body is denoted as $\mathcal{B}_0$ at time $t = t_0$ and the deformed configuration as $\mathcal{B}_1$ at time t_1.

Let $\boldsymbol{x}'$ denote the position of a particular material particle belonging to $\mathcal{H}_x$, and $\boldsymbol{\xi} = \boldsymbol{x}' - \boldsymbol{x}$ denote a bond between the respective material particle at $\boldsymbol{x}'$ and the center particle at $\boldsymbol{x}$. The deformation vector state, indicated as $\underline{\boldsymbol{Y}}[\boldsymbol{x}, t]\langle \boldsymbol{x}' - \boldsymbol{x}\rangle$, maps the bond $\boldsymbol{\xi}$ in the reference configuration to its deformed counterpart, i.e., $\underline{\boldsymbol{Y}}[\boldsymbol{x}, t]\langle \boldsymbol{x}' - \boldsymbol{x}\rangle = \boldsymbol{y}' - \boldsymbol{y}$. The corresponding deformation gradient tensor $\boldsymbol{F}(\boldsymbol{x}, t)$ can be defined in terms of $\underline{\boldsymbol{Y}}[\boldsymbol{x}, t]\langle \boldsymbol{x}' - \boldsymbol{x}\rangle$ as follows:

$$\boldsymbol{F}(\boldsymbol{x}, t) = \left(\int_{\mathcal{H}_x} \omega(\underline{\boldsymbol{Y}}[\boldsymbol{x}, t]\langle \boldsymbol{x}' - \boldsymbol{x}\rangle \otimes \boldsymbol{\xi})\, \mathrm{d}V_{\boldsymbol{x}'} \right) \boldsymbol{K}^{-1}(\boldsymbol{x}) \tag{1}$$

where ω is a weight function, quantifying the impact of neighboring particles on the center particle at $\boldsymbol{x}$. Here, the weight function ω can be selected as a radially symmetric parameter based on the initial bond length, i.e., $\omega = \omega(|\boldsymbol{\xi}|)$. Also, $\boldsymbol{K}(\boldsymbol{x})$ is a symmetric, positive-definite shape tensor, defined as:

$$\boldsymbol{K}(\boldsymbol{x}) = \int_{\mathcal{H}_x} \omega(\boldsymbol{\xi} \otimes \boldsymbol{\xi})\, \mathrm{d}V_{\boldsymbol{x}'} \tag{2}$$

Therefore, the governing equations of state-based PD at time t can be formulated as follows:

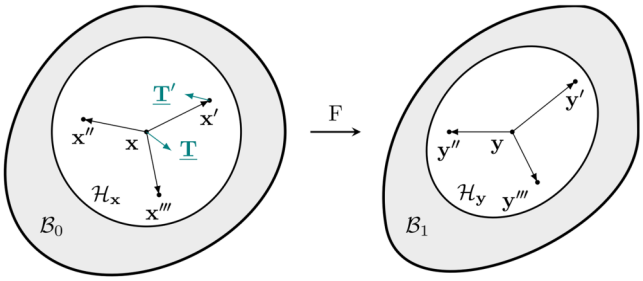

Fig. 2 Kinematics of non-ordinary state-based PD. $\mathcal{B}_0$ denotes the reference configuration of the body, while $\mathcal{B}_1$ is the deformed configuration. The particle at x is bonded to its neighboring particles, located at x', x'', and x''', within a finite region $\mathcal{H}_x$. The body deforms, so the particle at x displaces to y. The mapping can be described by the corresponding deformation gradient $F(x,t)$. $\underline{T} = \underline{T}[x,t]\langle x' - x\rangle$ and $\underline{T'} = \underline{T}[x',t]\langle x - x'\rangle$ are force vector states in the reference configuration for particles locating at x and x', respectively. In the non-ordinary state-based PD theory, these two force vectors are not necessarily parallel and can be obtained from the classical stress tensor.

$$\rho \ddot{\boldsymbol{u}}(\boldsymbol{x}, t) = \boldsymbol{L}(\boldsymbol{x}, t) + \boldsymbol{b}(\boldsymbol{x}, t)$$
$$\boldsymbol{L}(\boldsymbol{x}, t) = \int_{\mathcal{H}_x} (\underline{\boldsymbol{T}}[\boldsymbol{x}, t]\langle \boldsymbol{x}' - \boldsymbol{x}\rangle - \underline{\boldsymbol{T}}[\boldsymbol{x}', t]\langle \boldsymbol{x} - \boldsymbol{x}'\rangle)\, \mathrm{d}V_{\boldsymbol{x}'} \tag{3}$$

where $\underline{\boldsymbol{T}}[\boldsymbol{x}, t]\langle \boldsymbol{x}' - \boldsymbol{x}\rangle$ is a force vector state, operating on the bond $\boldsymbol{\xi}$ for the particle at position $\boldsymbol{x}$ and time t. Here, $\boldsymbol{L}(\boldsymbol{x}, t)$ is the summation of the forces per unit reference volume due to the interactions of the particle at location $\boldsymbol{x}$ with its neighboring particles inside the self-centered horizon $\mathcal{H}_x$. Furthermore, vector $\boldsymbol{b}(\boldsymbol{x}, t)$ denotes the body force density corresponding to the material particle at $\boldsymbol{x}$ and time t, while ρ refers to the material density.

In correspondence with the classical continuum theories, the force state $\underline{\boldsymbol{T}}[\boldsymbol{x}, t]\langle \boldsymbol{x}' - \boldsymbol{x}\rangle$ is related to the first Piola–Kirchoff (PK-I) stress tensor, denoted as $\boldsymbol{P}(\boldsymbol{x}, t)$, via the following equation:

$$\underline{\boldsymbol{T}}[\boldsymbol{x}, t]\langle \boldsymbol{x}' - \boldsymbol{x}\rangle = \omega \boldsymbol{P}(\boldsymbol{x}, t) \boldsymbol{K}^{-1}(\boldsymbol{x}) \boldsymbol{\xi} \tag{4}$$

Hence, $\boldsymbol{P}(\boldsymbol{x}, t)$ can be computed from a classical constitutive model using the deformation gradient $\boldsymbol{F}(\boldsymbol{x}, t)$. Compared with the governing equations of classical continuum mechanics, no spatial derivative appears in Eq. (3). This places fewer restrictions on the regularity properties of deformation descriptors. Furthermore, it is worth noting that despite the current PD model being non-ordinary, the balance of angular momentum is ensured due to the relation in Eq. (4) [18,27].

In this paper, an explicit dynamic relaxation method with the quasi-static assumption and a careful time-step selection, as outlined in the Appendix, is adopted. Nonlinear problems involving static solutions can alternatively be solved iteratively as a dynamic problem using artificial damping.

1. Numerical Discretization Scheme and Algorithm

Assume that there are N neighboring particles surrounding the central material particle located at $\boldsymbol{x}$, then Eq. (3) can be discretized for a specific time frame $t = t_n$ as in the following, while neglecting the body force $\boldsymbol{b}(\boldsymbol{x})$:

$$\boldsymbol{L}(\boldsymbol{x}) = \sum_{i=1}^{N} (\underline{\boldsymbol{T}}[\boldsymbol{x}]\langle \boldsymbol{x}_i' - \boldsymbol{x}\rangle - \underline{\boldsymbol{T}}[\boldsymbol{x}_i']\langle \boldsymbol{x} - \boldsymbol{x}_i'\rangle) V_{\boldsymbol{x}_i'} = \boldsymbol{0} \tag{5}$$

where $\boldsymbol{x}_i'$ is the location of the ith neighboring particle in $\boldsymbol{x}$'s horizon, and $V_{\boldsymbol{x}_i'}$ is its corresponding volume. Next, the deformation gradient $\boldsymbol{F}(\boldsymbol{x})$, for the material particle at $\boldsymbol{x}$ at the specific time frame $t = t_n$, can be discretized as:

$$\boldsymbol{F}(\boldsymbol{x}) = \left(\sum_{i=1}^{N} \omega_i (\boldsymbol{y}_i' - \boldsymbol{y}) \otimes (\boldsymbol{x}_i' - \boldsymbol{x}) V_{\boldsymbol{x}_i'} \right) \boldsymbol{K}^{-1}(\boldsymbol{x}) \tag{6}$$

where $\boldsymbol{y}'$ and $\boldsymbol{y}$ represent the images (i.e., the deformed positions) of material particles at $\boldsymbol{x}'$ and $\boldsymbol{x}$, respectively, and ω_i denotes the weight function of the ith particle within the horizon of the center particle at $\boldsymbol{x}$. Similarly, the shape tensor $\boldsymbol{K}(\boldsymbol{x})$ can be computed as

$$\boldsymbol{K}(\boldsymbol{x}) = \sum_{i=1}^{N} \omega_i (\boldsymbol{x}_i' - \boldsymbol{x}) \otimes (\boldsymbol{x}_i' - \boldsymbol{x}) V_{\boldsymbol{x}_i'} \tag{7}$$

Given the constitutive model, represented by an operator $\mathcal{F}$, the force states $\underline{\boldsymbol{T}}[\boldsymbol{x}]\langle \boldsymbol{x}_i' - \boldsymbol{x}\rangle$ for the particle at $\boldsymbol{x}$ and $\underline{\boldsymbol{T}}[\boldsymbol{x}_i']\langle \boldsymbol{x} - \boldsymbol{x}_i'\rangle$ for the particle at $\boldsymbol{x}'$, as found in Eq. (5), can be obtained from

$$\underline{\boldsymbol{T}}[\boldsymbol{x}]\langle \boldsymbol{x}_i' - \boldsymbol{x}\rangle = \omega_i \mathcal{F}(\boldsymbol{F}(\boldsymbol{x})) \boldsymbol{K}^{-1}(\boldsymbol{x})(\boldsymbol{x}_i' - \boldsymbol{x})$$
$$\underline{\boldsymbol{T}}[\boldsymbol{x}_i']\langle \boldsymbol{x} - \boldsymbol{x}_i'\rangle = \omega_i \mathcal{F}(\boldsymbol{F}(\boldsymbol{x}_i')) \boldsymbol{K}^{-1}(\boldsymbol{x}_i')(\boldsymbol{x} - \boldsymbol{x}_i') \tag{8}$$

Yet, in order to acquire $\boldsymbol{F}(\boldsymbol{x}_i')$ and $\boldsymbol{K}(\boldsymbol{x}_i')$ for the particle at $\boldsymbol{x}_i'$, information about the ith particle's horizon must be determined.

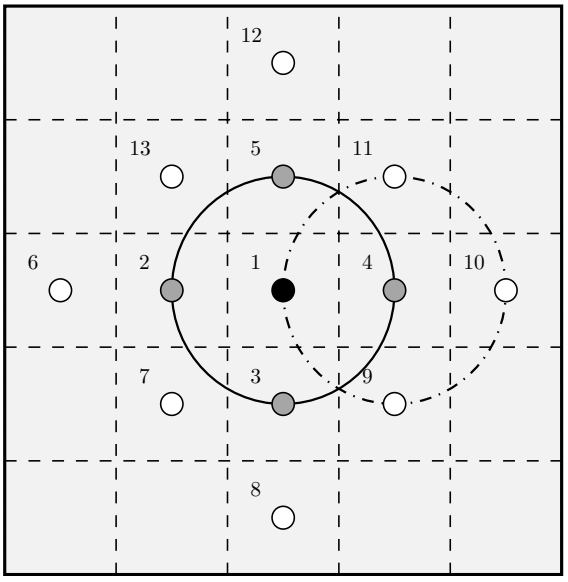

Fig. 3 Particle interactions with closest neighbors in a 2D PD model. Particles $i = 2, 3, 4, 5$ are the nearest neighbors of the particle 1 (denoted as the center particle at x); while particles $i = 1, 9, 10, 11$ are the nearest neighbors of the particle 4 (denoted as the particle at x_i'). In this case, all 13 particles shown above should be included in order to obtain $L(x)$ at particle x in Eq. (5).

Figure 3 is an illustration of interactions of one particle with its nearest neighbors in a 2D material domain.

With all force vector states obtained, the adaptive dynamic relaxation scheme (ADRS), as elaborated in the Appendix, is applied to solve the equation $\boldsymbol{L}(\boldsymbol{x}) = \boldsymbol{0}$. For a 2D problem, the global equation of motion can be organized as a vector system with a size of $2 \times N_{\text{total}}$, where N_{total} is the total number of particles in the simulation. Because $\boldsymbol{L}(\boldsymbol{x})$ is completely dependent on the current field, the system can be explicitly started with an initial guess of displacement, velocity, and acceleration fields. During dynamic iterations in one loading step, two absolute errors, denoted as ε_1 and ε_2, are calculated at each iteration with the definitions as:

$$\varepsilon_1 = \frac{\|\boldsymbol{L}(\boldsymbol{x})\|_2}{N_{\text{total}}} \quad \text{and} \quad \varepsilon_2 = \frac{\|\delta \boldsymbol{u}\|_2}{N_{\text{total}}} \tag{9}$$

where $\|.\|_2$ denotes a Euclidean norm. The first error ε_1 describes the degree to which $\boldsymbol{L}(\boldsymbol{x})$ approaches zero, whereas the second error ε_2 denotes the magnitude of displacement increments between two adjacent iteration steps. To normalize the error from initial guesses, two corresponding relative errors e_1 and e_2 are then monitored, as computed below:

$$e_1 = \frac{\varepsilon_1}{\varepsilon_1^0} \quad \text{and} \quad e_2 = \frac{\varepsilon_2}{\varepsilon_2^0} \tag{10}$$

where ε_1^0 and ε_2^0 are the initial absolute errors in each loading step. Iterations stop only when both criteria are satisfied, i.e., $e_{1,2} < e_l$ with $e_l = 10^{-6}$. All quantities are then updated into the next loading step. To improve the computational performance, parallel libraries such as OpenMP and Open MPI are adopted in the code. Given that kinematic properties, such as the displacement $\boldsymbol{u}$ and deformation gradient $\boldsymbol{F}$, are known beforehand due to use of an explicit method, the constitutive model can be applied on different particles in parallel. In other words, the computation involved in acquiring $\boldsymbol{P}(\boldsymbol{x}) = \mathcal{F}(\boldsymbol{F}(\boldsymbol{x}))$ and $\boldsymbol{P}(\boldsymbol{x}') = \mathcal{F}(\boldsymbol{F}(\boldsymbol{x}'))$ corresponding to the material particles at $\boldsymbol{x}$ and $\boldsymbol{x}'$, respectively, is completely independent. The computation domain is therefore partitioned into several groups in order to parallelize the calculation of the stress tensors. Finally, all information is gathered in the assembly of the vector system $\boldsymbol{L}(\boldsymbol{x})$. The flowchart in Fig. 4 summarizes the important numerical steps within the non-local state-based PD scheme described above.

In the presented PD framework, a crystal elastoplasticity model with deformation twinning is incorporated, where a generalized Hooke's law characterizes the elastic behavior of the microstructure and is accompanied by a rate-independent CP formulation to model the plastic constitutive behavior [14]. The rate-independent CP constitutive model implementation is elaborated in detail in [29].

B. Zero-Energy Modes

The PD technique used in this paper incorporates a correspondence material model in determining the bond forces from the PK-I stress tensor. The inherent stability issue of zero-energy modes is essentially the result of non-unique mapping between deformation states and force states via the PD deformation gradient tensor [30,40,41,47]. To better understand the origin of zero-energy numerical oscillations, a simple example is discussed next. Consider a 2D uniform lattice as illustrated in Fig. 5, where $\boldsymbol{x}$ and $\boldsymbol{x}'$ indicate the positions of the central material particle and one of its neighbors, respectively, at the original configuration. Let $\boldsymbol{F}_{\text{old}}(\boldsymbol{x}, t)$ denote the initial deformation gradient, while $\boldsymbol{F}_{\text{new}}(\boldsymbol{x} + \boldsymbol{u}_d, t)$ represents the deformation gradient after a small displacement disturbance $\boldsymbol{u}_d$, applied to the center particle at $\boldsymbol{x}$. The new deformation gradient $\boldsymbol{F}_{\text{new}}(\boldsymbol{x} + \boldsymbol{u}_d, t)$ can be then calculated based on Eq. (1) as

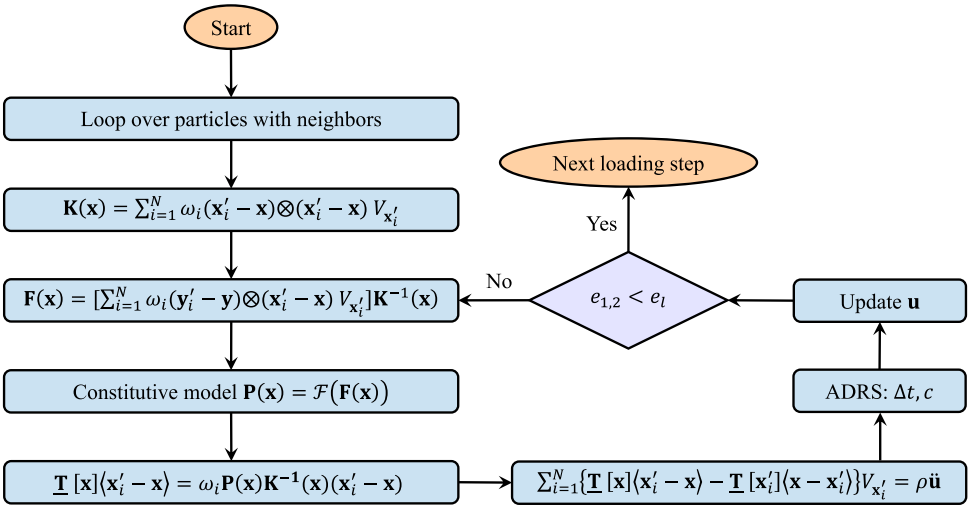

Fig. 4 Flowchart for the explicit non-local state-based PD scheme using ADRS.

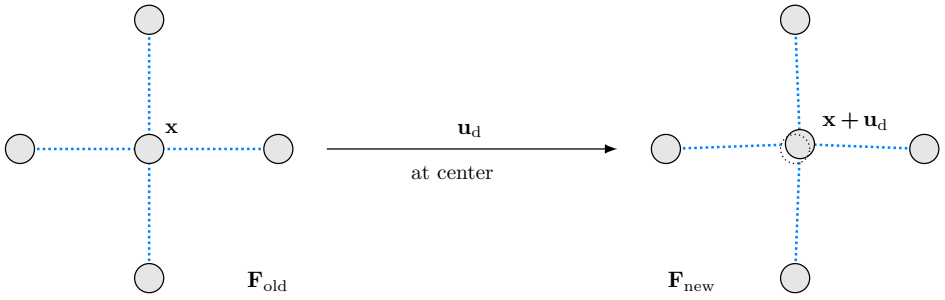

Fig. 5 An illustration of zero-energy modes in a 2D regular lattice. A small disturbance applied to the center particle has no impact on the calculation of the deformation gradient.

$$\begin{aligned}
&\boldsymbol{F}_{\text{new}}(\boldsymbol{x}+\boldsymbol{u}_d,t)\\
&=\left(\int_{\mathcal{H}_x}\omega(\underline{\boldsymbol{Y}}_{\text{new}}[\boldsymbol{x}+\boldsymbol{u}_d,t]\langle\boldsymbol{x}'-\boldsymbol{x}-\boldsymbol{u}_d\rangle\otimes\boldsymbol{\xi})\,\mathrm{d}V_{\boldsymbol{x}'}\right)\boldsymbol{K}^{-1}(\boldsymbol{x})\\
&=\left(\int_{\mathcal{H}_x}\omega[(\underline{\boldsymbol{Y}}_{\text{old}}[\boldsymbol{x},t]\langle\boldsymbol{x}'-\boldsymbol{x}\rangle-\boldsymbol{u}_d)\otimes\boldsymbol{\xi}]\,\mathrm{d}V_{\boldsymbol{x}'}\right)\boldsymbol{K}^{-1}(\boldsymbol{x})\\
&=\boldsymbol{F}_{\text{old}}(\boldsymbol{x},t)-\boldsymbol{u}_d\otimes\left(\int_{\mathcal{H}_x}\omega\boldsymbol{\xi}\,\mathrm{d}V_{\boldsymbol{x}'}\right)\boldsymbol{K}^{-1}(\boldsymbol{x})
\end{aligned}\tag{11}$$

With the assumption of a regular lattice discretization and a spherically symmetric influence function ω, the integration term on the right-hand side becomes zero. This is the case of admissible displacement fields producing the same deformation gradient and potential energy, which is appropriately called the zero-energy mode. This is a common stability issue when using correspondence material methods with mesh-free discretizations [54,55].

In Sec. II.C, a thorough discussion on the accuracy and stability of an explicit numerical scheme, termed "higher-order approximation theory," toward the elimination of the zero-energy mode oscillations is described.

C. Higher-Order Approximation Theory

The higher-order approximation method was initially proposed in Yaghoobi and Chorzepa [30] for 2D lattice structures and later enhanced in Javaheri et al. [56]. The basic idea is to adjust the influence weight functions based on a Taylor series expansion to better approximate the deformation gradient. This approach is shown to be highly effective in suppressing spurious zero-energy mode oscillations. In addition, higher-order approximations are easily implementable within the state-based PD framework, where larger horizon sizes can be used.

In the continuum mechanics, the relation between the deformed bond $\delta\boldsymbol{y}=\boldsymbol{y}'-\boldsymbol{y}$ and the reference bond $\delta\boldsymbol{x}=\boldsymbol{x}'-\boldsymbol{x}$, as illustrated in Fig. 2, can be expressed via the Taylor series expansion, as follows:

$$\boldsymbol{y}'-\boldsymbol{y}=\frac{\partial\boldsymbol{y}}{\partial\boldsymbol{x}}(\boldsymbol{x}'-\boldsymbol{x})+O[(\boldsymbol{x}'-\boldsymbol{x})^2]\tag{12}$$

where the notation O denotes the order of the leading error term. Here, $\partial\boldsymbol{y}/\partial\boldsymbol{x}$ is equivalent to the deformation gradient tensor. To incorporate the state-based PD deformation gradient, a tensor product on the reference bond $\boldsymbol{x}'-\boldsymbol{x}$ is first performed on both sides of Eq. (12), and the result is then integrated over the initial horizon $\mathcal{H}_{\boldsymbol{x}}$, as follows:

$$\begin{aligned}
\int_{\mathcal{H}_x}\omega[(\boldsymbol{y}'-\boldsymbol{y})\otimes(\boldsymbol{x}'-\boldsymbol{x})]\,\mathrm{d}V_{\boldsymbol{x}'}=\int_{\mathcal{H}_x}\frac{\partial\boldsymbol{y}}{\partial\boldsymbol{x}}\omega[(\boldsymbol{x}'-\boldsymbol{x})\otimes(\boldsymbol{x}'-\boldsymbol{x})]\,\mathrm{d}V_{\boldsymbol{x}'}\\
+O[(\boldsymbol{x}'-\boldsymbol{x})^3]
\end{aligned}\tag{13}$$

Therefore, the deformation gradient tensor at time t can be approximated by:

$$\begin{aligned}
\boldsymbol{F}(\boldsymbol{x},t)=\frac{\partial\boldsymbol{y}}{\partial\boldsymbol{x}}=\left(\int_{\mathcal{H}_x}\omega[(\boldsymbol{y}'-\boldsymbol{y})\otimes(\boldsymbol{x}'-\boldsymbol{x})]\,\mathrm{d}V_{\boldsymbol{x}'}\right)\boldsymbol{K}^{-1}(\boldsymbol{x})\\
+O(\boldsymbol{x}'-\boldsymbol{x})
\end{aligned}\tag{14}$$

Once the error term, i.e., $O(\boldsymbol{x}'-\boldsymbol{x})$, is eliminated, Eq. (14) becomes the same as Eq. (1), where $\boldsymbol{K}(\boldsymbol{x})$ is defined as the shape tensor in the state-based PD model. Note that the leading error term in Eq. (14) is of the first order of the distance between material particles located at $\boldsymbol{x}'$ and $\boldsymbol{x}$. To achieve a more accurate deformation gradient, appropriate influence function values ω for the required horizon can be chosen to artificially increase the leading error order. This is explained for multi-dimensional domains in Sec. II.C.1. The specific contribution area of this paper is the development of a set of higher-order tensor equations to efficiently identify the constraint formulations for the influence weight functions when using higher-order approximation method.

1. *Multi-Dimensional Discrete Formulation*

Hereon, the multi-dimensional Taylor series expansion is applied for deriving weight function values ω across 1D, 2D, and 3D material domains with a constant particle spacing h for $\delta\le 3h$, where δ denotes the interacting horizon radius. This paper incorporates a uniform particle discretization, i.e., equally spaced particles along a line in 1D, quadrilateral discretizations in 2D, or cubic patterns in 3D having a constant particle spacing h with a fixed particle volume ΔV. Accordingly, the influence function values ω are always assumed to be spherically symmetric, i.e., $\omega=\omega(|\boldsymbol{\xi}|)$. For the sake of simplicity, the Einstein tensor notation is adopted in the following discussion. The shape tensor $\boldsymbol{K}(\boldsymbol{x})$ in Eq. (2) and the deformation gradient tensor $\boldsymbol{F}(\boldsymbol{x},t)$ in Eq. (1) can alternatively be expressed in Einstein notation as follows:

$$K_{ij}=\int_{\mathcal{H}_x}\omega\delta x_i\delta x_j\,\mathrm{d}V_{\boldsymbol{x}'}\tag{15}$$

$$F_{pq}=\left(\int_{\mathcal{H}_x}\omega\delta y_p\delta x_j\,\mathrm{d}V_{\boldsymbol{x}'}\right)K^{-1}_{jq}\tag{16}$$

Due to the symmetric nature of the particle discretizations, the shape tensor in Eq. (15) can be reformulated as:

$$K_{ij}=\sum_{a=1}^{N}\omega_a(\delta x_i\delta x_j)_a\Delta V=\Omega(\omega_1,\omega_2,\omega_3,\dots)h^2\Delta V\delta_{ij}\tag{17}$$

where N is the total number of neighboring material particles within the horizon $\mathcal{H}_{\boldsymbol{x}}$, δ_{ij} is the Kronecker delta function, and Ω is a function of all independent $\omega_1,\omega_2,\dots,\omega_N$ in the horizon. For instance, consider a 2D quadrilateral particle discretization as depicted in Fig. 6, with a horizon size $\delta=2h$. While there are a total of 12 neighboring material particles within the given horizon radius $\delta=2h$, due to the radially symmetric nature of discretization pattern, only three independent weight function values are labeled, i.e., $\omega_1=\omega(h)$, $\omega_2=\omega(\sqrt{2}h)$, and $\omega_3=\omega(2h)$.

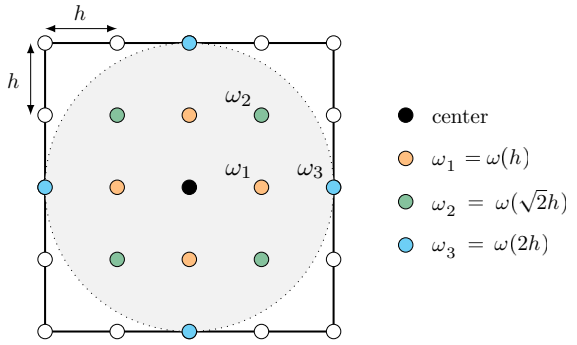

Fig. 6 Independent weight function values on a 2D quadrilateral particle pattern. Here, ω is a radially symmetric weight function on neighboring material particles. The horizon radius is $\delta = 2h$, with h denoting the distance between nearest particles.

Consequently, by substituting Eq. (17) into Eq. (16), the deformation gradient can be reformulated as:

$$F_{pq} = \frac{\delta_{jq}}{h^2\Omega\Delta V}\int_{\mathcal{H}_x} \omega\delta y_p \delta x_j \, \mathrm{d}V_{x'} = \frac{1}{h^2\Omega}\sum_{a=1}^{N}\omega_a(\delta y_p \delta x_q)_a \quad (18)$$

Accordingly, a multi-dimensional Taylor series expansion of the deformed bond $\delta\boldsymbol{y}$ on the reference bond $\delta\boldsymbol{x}$ is required. The first three leading terms are shown here without showing the derivations:

$$\delta y_p = F_{pi}\delta x_i + \frac{1}{2!}G_{pij}\delta x_i\delta x_j + \frac{1}{3!}H_{pijk}\delta x_i\delta x_j\delta x_k + O(h^4) \quad (19)$$

where $F_{pi} = (\partial\delta y_p/\partial\delta x_i)$ is the deformation gradient; $G_{pij} = (\partial^2\delta y_p/\partial\delta x_i\delta x_j)$ and $H_{pijk} = (\partial^3\delta y_p/\partial\delta x_i\delta x_j\delta x_k)$ are the second-order and third-order derivatives, respectively.

Finally, by substituting Eq. (19) into Eq. (18), the deformation gradient then turns into:

$$F_{pq} = F_{pq} + \frac{1}{2!h^2\Omega}G_{pij}\sum_{a=1}^{N}\omega_a(\delta x_i\delta x_j\delta x_q)_a + \frac{1}{3!h^2\Omega}H_{pijk}\sum_{a=1}^{N}\omega_a(\delta x_i\delta x_j\delta x_k\delta x_q)_a + O(h^3) \quad (20)$$

Accordingly, it is possible to achieve higher-order approximations by selecting explicit weight functions in Eq. (20). It is worth noting that in a spherically symmetric and intact discretization, for every bond $(\delta\boldsymbol{x})_m$, there is another bond $(\delta\boldsymbol{x})_n$ symmetric about the origin such that $(\delta\boldsymbol{x})_m = -(\delta\boldsymbol{x})_n$. Hence, when there are odd δx products, the summation terms in Eq. (20) become:

$$\sum_{a=1}^{N}\omega_a(\delta x_i\delta x_j\ldots\delta x_m)_a = 0 \quad (21)$$

As odd δx-product summations vanish, symmetric particle patterns with intact horizons always lead to accuracy order equal or greater than $O(h^2)$. One additional equation, as formulated below, needs to be satisfied to obtain a higher truncation error in the order of $O(h^4)$:

$$A_{ijkl} = \sum_{a=1}^{N}\omega_a(\delta x_i\delta x_j\delta x_k\delta x_l)_a = 0 \quad (22)$$

Furthermore, the satisfaction of the following two equations leads to higher accuracy, in the order of $O(h^6)$:

$$\begin{cases} A_{ijkl} = \sum_{a=1}^{N}\omega_a(\delta x_i\delta x_j\delta x_k\delta x_l)_a = 0 \\ B_{ijklrs} = \sum_{a=1}^{N}\omega_a(\delta x_i\delta x_j\delta x_k\delta x_l\delta x_r\delta x_s)_a = 0 \end{cases} \quad (23)$$

Criteria outlined in Eqs. (22) and (23) hold true regardless of the material dimensions, i.e., 1D line, 2D quadrilateral, or 3D cubic patterns. The final selection of weight function values should satisfy the constraint inequality $\Omega(\omega_1, \omega_2, \omega_3, \ldots) \neq 0$ to ensure that the shape tensor $\boldsymbol{K}(\boldsymbol{x})$ obtained in Eq. (17) is invertible. It is worth noting that larger horizon sizes with more independent weight function values often lead to increased orders of truncation error.

The weight function values for a 1D particle-discretized bar with a constant spacing h and horizon sizes up to $\delta = 4h$ are tabulated in Table 1. For the sake of simplicity and unity, the weight function value corresponding to the particle closest to the center particle is set to be 1, i.e., $\omega_1 = 1$. Additionally, the order of leading truncation error increases when the horizon size δ grows, providing a more accurate deformation gradient. For a 1D bar with a horizon $\delta = 2h$ as depicted in Fig. 7, there are five material particles at x_{i+j} for $j = 0, \pm1, \pm2$ with only two independent weight functions ω_1 and ω_2, pertaining to particles at $x_{i\pm1}$ and $x_{i\pm2}$, respectively. Hence, setting $\omega_1 = 1$ and $\omega_2 = -1/16$ produces a fourth-order leading error of the form $O(h^4)$ in the Taylor series expansion of the deformation gradient in Eq. (20) when $\delta = 2h$.

Next is a brief discussion on the number of nontrivial components in the fourth-order tensor A_{ijkl} for a 2D quadrilateral discretization pattern. First of all, it is worth noting that the subscript indices can be swapped as follows:

$$A_{ijkl} = A_{jikl} = A_{ijlk} \quad (24)$$

Consequently, in the case of 2D quadrilateral particle pattern, where subscript indices can only take on values 1 and 2, only six components of tensor A_{ijkl} are independent. These independent elements are $A_{1111}, A_{2111}, A_{2211}, A_{2221}$, and A_{2222}.

Secondly, due to the axis symmetry of the horizon and particle discretization, the coordinate index 1 and 2 can be swapped, yielding to the following two constraints:

$$A_{1111} = A_{2222} \quad \text{and} \quad A_{2111} = A_{1112} \quad (25)$$

Thirdly, assume that there is a bond with rectangular coordinates (x, y) and a weight function ω_1. Owing to the symmetry of coordinate axes, three other bonds with respective coordinates $(-x, y)$, $(-x, -y)$, and $(x, -y)$ are expected to be in the same horizon as well. Hence, based on the definition in Eq. (22), the A_{2221} entry becomes:

$$A_{2221} = \omega_1 y^2(xy - xy + xy - xy) = 0 \quad (26)$$

Table 1 Higher-order approximation weight functions for 1D particle discretization with a constant spacing h

	Weight function values				
Horizon size	ω_1	ω_2	ω_3	ω_4	Leading error
$\delta = h$	1	0	0	0	$O(h^2)$
$\delta = 2h$	1	−1/16	0	0	$O(h^4)$
$\delta = 3h$	1	−1/10	1/135	0	$O(h^6)$
$\delta = 4h$	1	−1/8	1/63	−1/896	$O(h^8)$

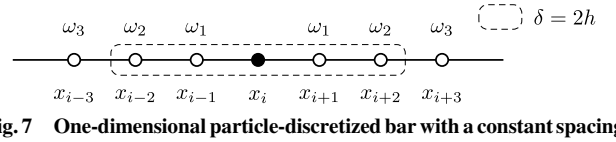

Fig. 7 One-dimensional particle-discretized bar with a constant spacing h. Here, ω is a symmetric weight function. Dashed box with $\delta = 2h$ illustrates the horizon of center particle x_i, including only the nearest four particles.

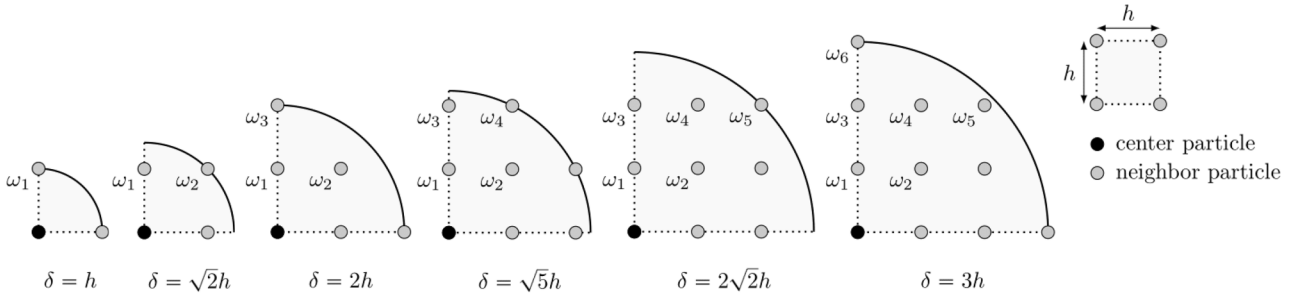

Fig. 8 All possible 2D horizon shapes with a quadrilateral particle discretization up to $\delta = 3h$. Because the weight function ω is radially symmetric, only a quarter of interacting circular regions are depicted for each horizon size δ.

Eventually, only two components of the fourth-order tensor A_{ijkl} are nonzero. These components are A_{1111} and A_{2211}.

Consistent with 1D discretizations, the weight function value corresponding to the particle closest to the center particle is set to be 1, i.e., $\omega_1 = 1$. To achieve $O(h^4)$, two more independent weight function values (i.e., ω_2 and ω_3) need to be calculated. Consequently, the horizon with radius $\delta = 2h$ in Fig. 8 is the smallest horizon size that can achieve a truncation error in the order of $O(h^4)$ in the 2D quadrilateral pattern. In terms of horizons with excess independent weight functions, but not enough to achieve higher-order truncation errors, the weight function values are generally not unique. These horizon selections could possibly bring noise or numerical oscillations to the ultimate solutions. As a result, the numerical simulations in Sec. III primarily focus on horizon sizes with unique weight function values, as tabulated in Tables 2 and 3. Typically, the magnitude of weight function values decrease from the closest particles to distant particles, and the value on the farthest particle should be a nonzero.

For 2D quadrilateral patterns, horizon sizes up to $\delta = 3h$ are studied. Figure 8 illustrates all possible spatial distributions of neighboring particles for different horizon sizes. Here, only a quarter of the interacting circular space is depicted due to the symmetric nature of material particle discretization. The unique weight function values for these horizon sizes are obtained using the following process. The constraint equations for the weight function values to achieve the desired leading error, such as Eqs. (22) and (23), are identified. These constraints typically lead to a multiple nonunique set of weight functions for a given horizon size δ. As such, additional equations from the next set of higher-order constraint equations that do not contain the ω_1 term are added to the existing set of constraint equations. The solution to such a constraint set leads to a unique set of weight function values for the specific material interaction. Table 2 shows these unique weight function values to achieve the corresponding higher-order accuracy for the 2D quadrilateral discretization. The constraint solutions that have either resulted in a zero influence function value at the material particle farthest from the center particle or led to a noninvertible shape tensor are excluded from Table 2.

Table 2 Higher-order approximation weight functions for a 2D quadrilateral discretization pattern with a constant spacing *h*

	Weight function values						
Horizon size	ω_1	ω_2	ω_3	ω_4	ω_5	ω_6	Leading error
$\delta = h$	1	0	0	0	0	0	$O(h^2)$
$\delta = 2h$	1	0	$-1/16$	0	0	0	$O(h^4)$
$\delta = 3h$	1	0	$-1/10$	0	0	1/135	$O(h^6)$

Here, horizon sizes in Fig. 8 that either encompass a zero influence function value at the farthest material particle within the given horizon radius or lead to a noninvertible shape tensor are excluded.

Similarly, for 3D cubic patterns, the horizon sizes up to $\delta \leq 3h$ are investigated, where h represents the spacing between nearest particles. Figure 9 illustrates all possible distributions of neighboring material particles for different horizon sizes δ. Here, similar to the 2D quadrilateral distribution, only a small portion of the interacting sphere is illustrated due to the symmetric nature of ω. Subsequently, a similar procedure as for 2D quadrilateral discretization is employed to derive the most optimal unique weight function values. Weight function values that either result in a zero value for the material particle farthest within the horizon shape or lead to a noninvertible shape tensor are disregarded in numerical simulations. Table 3 shows the unique weight function values to achieve corresponding higher accuracy for 3D cubic patterns.

D. Boundary Treatment

Conventional constraint conditions, such as Dirichlet and Neumann boundary conditions, are supposed to be imposed in different forms, as the PD governing equations are applied in non-local formulation. In the case of simulations with no boundary treatment, defect horizons can still approximate the deformation gradient across the boundary layer. However, as the horizon size δ increases, irregular defects ultimately lead to disordered and unstable solutions around the particles located at the margins. Because higher-order approximations are derived using the internal particles with a fully symmetric horizon, defect horizons along the external boundary are expected to give rise to numerical errors when approximating the deformation gradient. One possible solution, as suggested by Macek and Silling [57], is to apply an inward fictitious material layer along the boundary layer. As illustrated in Fig. 10a, the thickness or depth of the fictitious boundary layer should be equal to the horizon size δ, to ascertain that prescribed constraints are sufficiently enforced on the real material region. The same discretization spacing should be applied in both the fictitious boundary layer and real material domain.

Table 3 Higher-order approximation weight functions for a 3D cubic discretization pattern with a constant spacing *h*

	Weight function values								
Horizon size	ω_1	ω_2	ω_3	ω_4	ω_5	ω_6	ω_7	ω_8	Leading error
$\delta = h$	1	0	0	0	0	0	0	0	$O(h^2)$
$\delta = 2h$	1	0	0	$-1/16$	0	0	0	0	$O(h^4)$
$\delta = 3h$	1	$-80/267$	16/89	$-25/178$	14/267	$-8/267$	$-2/267$	1/267	$O(h^6)$

Here, horizon sizes in Fig. 9 that either encompass a zero influence function value at the farthest material particle within the given horizon radius or lead to a noninvertible shape tensor are excluded.

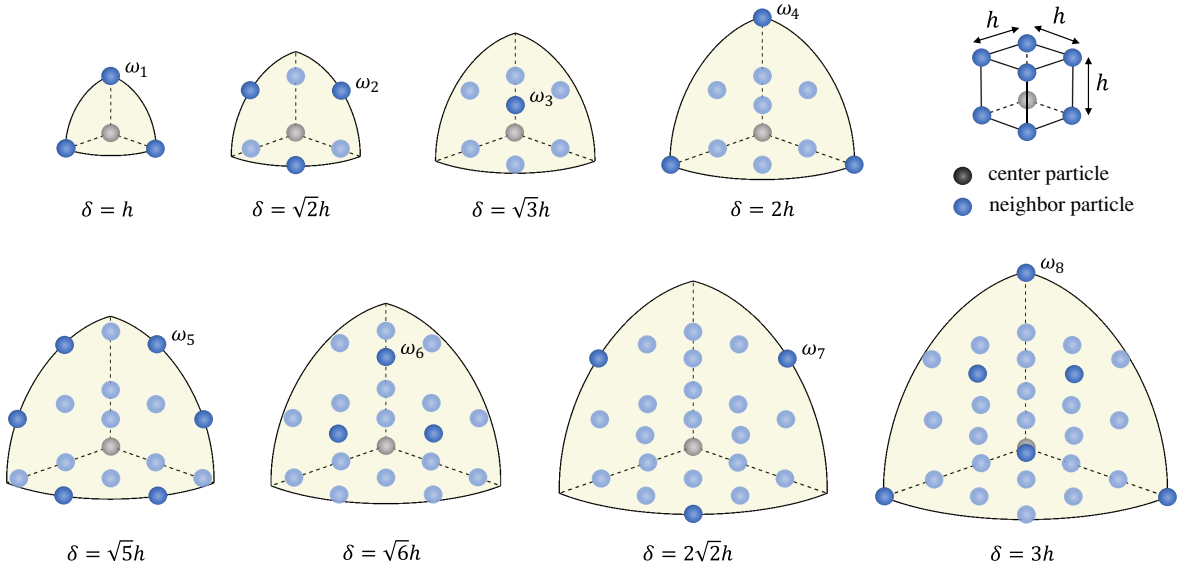

Fig. 9 All possible 3D horizon shapes with a cubic particle discretization up to $\delta = 3h$. Because the weight function ω is spherically symmetric, only one eighth of the interacting spherical regions are depicted for each horizon size δ.

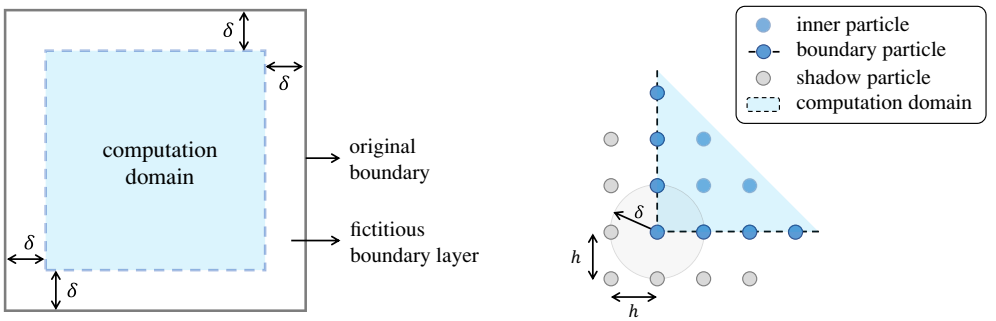

a) inward fictitious layer **b) shadow particles**

Fig. 10 Boundary treatment on a 2D polycrystalline domain. a) The fictitious boundary layer is inward possessing a thickness equal to the prescribed horizon radius δ. b) A horizon of $\delta = h$ is illustrated in this plot, where h is the particle spacing.

Shadow particles are therefore introduced in the fictitious layer, as shown in Fig. 10b.

Considering that no information is provided outside the original boundary, Madenci and Oterkus [21] suggested that the prescribed displacement vector should be the same as that of the closest material particle at the boundary. This operation results in zero strain and stress across the fictitious boundary layer. An alternative option is to apply a constant deformation gradient across the fictitious boundary layer. In this paper, displacements on shadow particles are prescribed based on a constant deformation gradient. Consequently, stress at shadow particles can be calculated by the correspondence constitutive model. This special boundary treatment has been particularly effective when larger-horizon interactions are applied, encompassing simulations beyond the nearest-neighbor PD family [41]. With such a boundary treatment procedure, all information (e.g., displacement and stress) on shadow particles is presumably known, in contrast with boundary particles where only displacement field is given [21].

III. Results and Discussion

Here, the non-local state-based PD algorithm is examined for a 1D elastic bar with a varying Young's modulus of elasticity. The resultant displacements of the PD scheme with the higher-order stabilization approach are compared against analytical solutions as well as numerical algorithms with no stability implementation. Thereafter, 2D and 3D numerical schemes are tested for different microstructures. Comparisons are performed against analytical and FEM solutions as needed. The examples aim to demonstrate that increasing the order of interactions in material particles can improve the accuracy of the numerical solution and reduce the hourglass instability modes of the non-local state-based PD framework.

A. One-Dimensional Cantilever Bar

The classic 1D cantilever elastic bar example [30,36,41], as depicted in Fig. 11a, is conducted for validation of the higher-order implementation. Here, the bar has a total length L_{tot} and a constant cross-sectional area A. Displacement constraints are applied on each side of the bar, i.e., $u(x = 0) = 0$ and $u(x = L_{\text{tot}}) = u_{\text{end}}$. In this 1D example, u_{end} is set to be $0.005L_{\text{tot}}$. A variable Young's modulus, as plotted in Fig. 11b, is also adopted as follows:

$$E(x) = \begin{cases} E_0 & 0 \le x \le L_{\text{tot}}/2 \\ E_0\left(1 + \dfrac{\beta}{2\alpha}\dfrac{1}{\sqrt{x/L_{\text{tot}} - 1/2}}\right)^{-1} & L_{\text{tot}}/2 < x \le L_{\text{tot}} \end{cases} \tag{27}$$

Consequently, the corresponding analytical displacement $u(x)$ can be computed to be as follows:

$$u(x) = \begin{cases} \alpha x & 0 \le x \le L_{\text{tot}}/2 \\ \alpha x + \beta L_{\text{tot}}\sqrt{x/L_{\text{tot}} - 1/2} & L_{\text{tot}}/2 < x \le L_{\text{tot}} \end{cases} \tag{28}$$

where parameters are set as $\alpha = 0.001$, $\beta = 0.004\sqrt{2}$, $L_{\text{tot}} = 1$, and $E_0 = 1$.

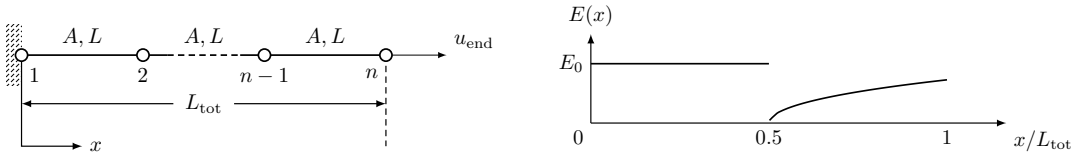

a) 1D elastic bar b) Variable Young's modulus

Fig. 11 One-dimensional cantilever bar. a) A one-dimensional elastic bar under tension with displacement constraints is used to study the effect of using higher-order approximations of deformation gradient. b) The example exhibits a varying Young's modulus along the x axis.

Subsequently, a uniform mesh with 500 equally distant material particles is employed to study the effect of using higher-order approximations framework on the resultant axial displacements $u(x)$, under outward displacement constraint $u_{\text{end}} = 0.005L_{\text{tot}}$. A comparison between the higher-order approximation solutions and those with no stabilization control method [52] is shown in Fig. 12. Because a higher-order approximation approach only takes effect in large-horizon families, i.e., $\delta > h$, two horizon selections $\delta = 2h$ and $\delta = 3h$ are illustrated in Fig. 12. As the horizon size increases, the hourglass oscillations grow dramatically if no control method is applied. In contrast, the higher-order approximation method suppresses the numerical oscillations in both cases (i.e., $\delta = 2h$ and $\delta = 3h$) and dampens the zero-energy modes effectively.

B. Two-Dimensional Polycrystalline Microstructure

Here, a 1×1 mm^2 polycrystalline microstructure with 21 grains, synthetically generated by Voronoi tessellation [3], is considered. In this example, 12 different orientation angles from the interval $[-\pi/2, \pi/2)$ are distributed randomly among grains. The discretized computational domain, as depicted in Fig. 13, is based on a uniform 50×50 particle discretization for PD technique, and 50×50 square-faced elements for FEM. With the number of particles being the same as the number of elements, the material particles in the PD model are located at the center of elements in the FE model. Consequently, each material particle occupies a constant area in the reference configuration that is equal to the corresponding enclosed FE area. Linear basis functions and traditional implicit solvers are employed in the FEM. Although different solvers are applied in PD and FE models, the same constraint on errors is set, i.e., $e_l = 10^{-6}$. The particular hardening law is chosen as follows [14]:

$$h^{\alpha\beta} = h_0^{\beta}(q + (1-q)\delta_{\alpha\beta})\left(1 - \frac{s^{\beta}(t)}{s_s^{\beta}}\right)^a \tag{29}$$

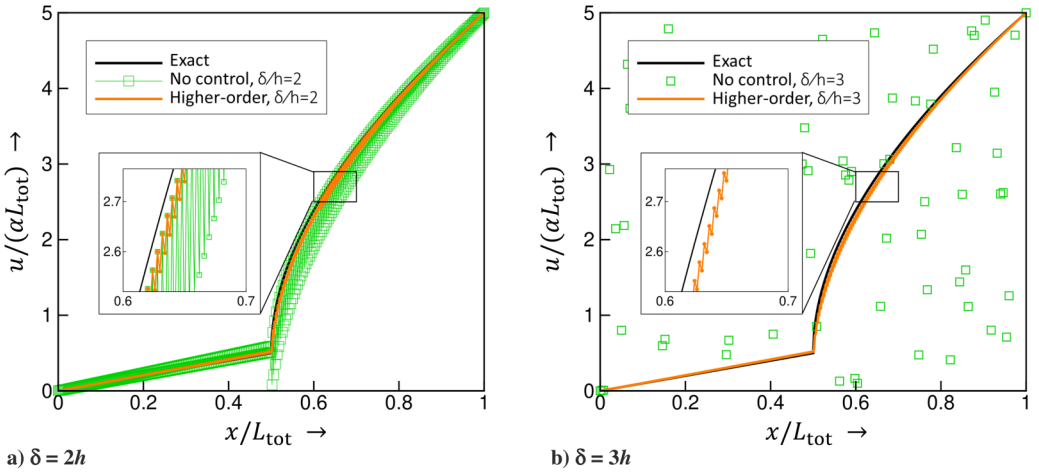

a) δ = 2h b) δ = 3h

Fig. 12 Effect of zero-energy modes on the displacement field of 1D bar obtained from the higher-order approximation approach with two different horizon sizes a) $\delta = 2h$ and b) $\delta = 3h$. Results are based on a uniform mesh with 500 material particles.

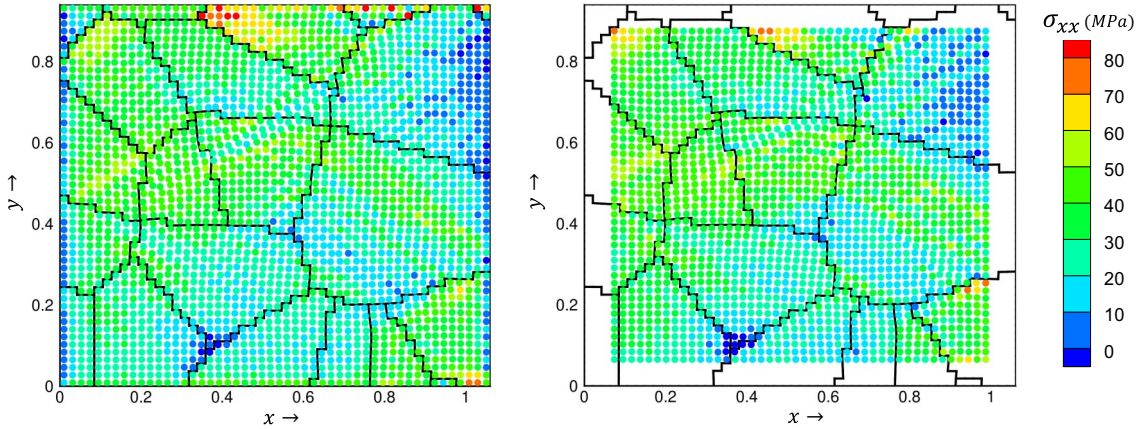

a) No boundary treatment b) Boundary enforcement

Fig. 13 The effect of boundary treatment on PD stress distributions with a horizon size $\delta = 3h$.

where h_0^β, $s^\beta(t)$, and s_s^β are the hardening coefficient, the current slip resistance, and the saturation resistance of slip system β, respectively; $\delta_{\alpha\beta}$ is the Kronecker delta function; and a and q are constant parameters. These hardening parameters are taken to be identical for both slip systems and are listed below:

$$h_0 = 10 \text{ MPa}, \qquad s(0) = 10 \text{ MPa}, \qquad s_s = 200 \text{ MPa},$$
$$a = 2, \qquad q = 1.4 \tag{30}$$

where $s(0)$ is the initial value of slip system resistance. Furthermore, a compression velocity gradient, as shown below, with plane strain assumptions is applied on microstructure boundaries to simulate the process of y-axis compression:

$$\boldsymbol{L} = \eta \begin{bmatrix} 1 & 0 \\ 0 & -1 \end{bmatrix} \tag{31}$$

where $\eta = 0.0020$ denotes a constant strain rate. Each simulation is performed over 30 steps with the corresponding velocity gradient leading to a final strain around 0.06. The isotropic elastic stiffness matrix is taken as $C_{11} = 2$, $C_{12} = 1$, and $C_{33} = 2$ (in gigapascals).

The inward boundary treatment, as elaborated in Sec. II.C, is then applied to constrain the velocity gradient of the fictitious boundary particles to that shown in Eq. (31) for the PD model. As the horizon radius δ grows, the boundary-layer thickness (equal to the horizon radius) increases, and the number of material particles within the computational domain decreases. Figure 13 provides an example illustrating the effect of enforcing the inward boundary treatment. In Fig. 13a, low-magnitude stress values are captured around the external edges without the fictitious boundary layer. This is mainly because of the erroneous deformation gradient approximated by the defect horizons. In contrast, the stress field obtained from the boundary enforcement, as depicted in Fig. 13b, shows no spurious values along the four outermost edges.

Next, Fig. 14 provides a comparison of the PD and FE techniques for modeling crystal orientation changes of the same polycrystal under a y-axis compression test, using three different horizon selections in Table 2. In the following, the quantification of the crystal orientation changes is briefly explained. In 2D polycrystals, each grain can be characterized by a rotation tensor, denoted as $\boldsymbol{R}$, relating the local crystal lattice frame to the reference sample frame. Given an orientation θ (i.e., the angle between crystal and sample axes), the associated rotation matrix supports parameterization as $\boldsymbol{R} = \cos(\theta)\boldsymbol{I} - \sin(\theta)\boldsymbol{E}$, where $\boldsymbol{E}$ is a 2D alternator (i.e., $E_{11} = E_{22} = 0$, $E_{12} = -E_{21} = 1$) and $\boldsymbol{I}$ is a 2D identity tensor. Consequently, the rotation tensor can be evaluated through a polar decomposition of the elastic deformation gradient as $\boldsymbol{F} = \boldsymbol{RU}$. The spin tensor $\boldsymbol{\Phi}$ can then be expressed as $\boldsymbol{\Phi} = \boldsymbol{RR}^T = -\dot{\theta}\boldsymbol{E}$, where $\dot{\theta} = (\partial\theta/\partial t)$ is the crystal reorientation velocity. Alternatively, in the component form, the crystal reorientation velocity can be expressed as $\dot{\theta} = (\Phi_{21} - \Phi_{12})/2$. Accordingly, using the reorientation velocity, the crystal texturing is tracked by $\Delta\theta = \dot{\theta}\Delta t$ at each time step.

Reorientation of grains predicted by PD and FE models are compared in Fig. 14 at the final strain value of 0.06. The overall reorientation contours, and locations of the shear bands are mostly similar between the two models at the same degree of mesh refinement. The localized shear bands seen from FE simulations are comparatively more diffuse due to the lack of an internal length scale. Along the direction of arrows, the width of a shear band obtained by PD simulations is smaller, and its boundary is more conspicuous, which are qualitatively closer to those seen in experiments [18,58–60]. It is clear from Fig. 14 that zero-energy modes are effectively suppressed in all long-range horizon selections. This is in agreement with the 1D elastic bar tension test seen previously in Sec. III.A, where the higher-order stabilization implementations are compared against the solutions with no stabilization control.

Additionally, as evident from PD simulations in Fig. 14, larger horizon interactions make the reorientation results more stable. Nevertheless, it is shown by Yaghoobi and Chorzepa [30] that by including more neighboring particles the higher-order approximation framework may lead to less stable results if the increased horizon size is not able to obtain a greater accuracy (e.g., $\delta = h$ vs. $\delta = \sqrt{2}h$). This is different from the 1D bar test in Sec. III.A, in which larger horizon sizes consistently reduced the spurious zero-energy mode oscillations.

C. Three-Dimensional Matrix with Soft Precipitate

For the first 3D example, a cubic matrix of dimensions $3 \times 3 \times 3$ mm^3 along with a central spherical precipitate with a diameter 0.875 mm having a lower modulus, as illustrated in Fig. 15, is modeled using both FE and PD techniques. The transversely isotropic elastic matrix is assigned with the following stiffness constants: $C_{11}^{\text{mat}} = 59.3$, $C_{12}^{\text{mat}} = 25.7$, $C_{13}^{\text{mat}} = 21.4$, $C_{33}^{\text{mat}} = 61.5$, and $C_{44}^{\text{mat}} = 16.4$ (in gigapascals). Contrarily, the stiffness constants assigned to the spherical precipitate are reduced by a factor of 10, i.e., $C_{ij}^{ppt} = 0.1 \times C_{ij}^{\text{mat}}$, where C_{ij}^{ppt} denotes the (i, j) entry of the elastic stiffness tensor pertaining to the precipitate particles. Here, both materials are assumed to be elastic under a small deformation. Thus, the strain tensor is computed as $\epsilon = (1/2)(\boldsymbol{F} + \boldsymbol{F}^T) - \boldsymbol{I}$, where $\boldsymbol{I}$ is the identity tensor. Also, Cauchy stress tensor $\sigma = \boldsymbol{C}{:}\epsilon$ is used in lieu of $\boldsymbol{P}$ in Eq. (4), assuming a small deformation, where $\boldsymbol{C}$ represents the elastic stiffness tensor.

The cubic material domain represented in Fig. 15a is discretized into a $48 \times 48 \times 48$ structured particle grid. A similar discretization refinement is adopted for the FE simulation, where each linear hexahedral volumetric element encompasses the material particle in the PD model. In addition, Dirichlet boundary conditions dictated by the following diagonal velocity gradient are applied to the microstructure boundaries to simulate an x-axis tension up to 0.02 strain:

$$\boldsymbol{L} = \begin{bmatrix} 1.0 & 0 & 0 \\ 0 & -0.5 & 0 \\ 0 & 0 & -0.5 \end{bmatrix} \tag{32}$$

Subsequently, numerical PD simulations are carried out using the higher-order influence weight functions tabulated in Table 3 for

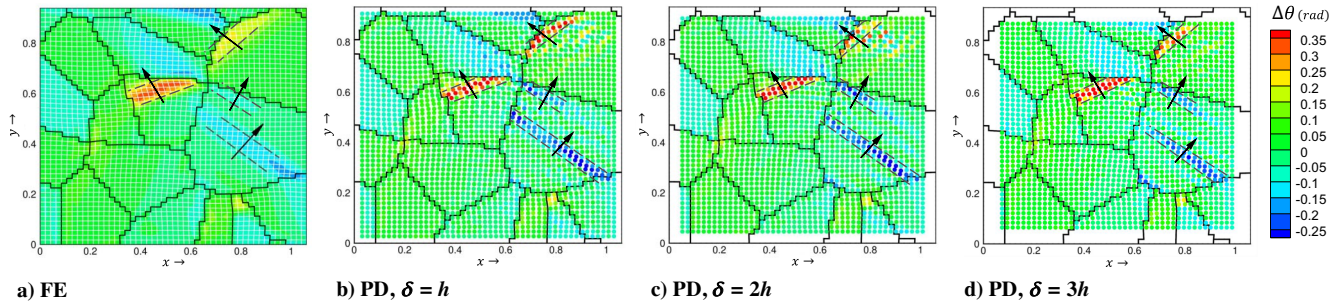

a) FE b) PD, $\delta = h$ c) PD, $\delta = 2h$ d) PD, $\delta = 3h$

Fig. 14 Orientation changes for 2500 particles under a y-axis compression test for FE and PD results with three different horizon sizes at final strain of 0.06. Along the direction of arrows, sharper and more number of shear bands can be seen in PD results. Here, δ is the horizon radius, and h is the distance between the nearest material particles. The margin around the boundary in PD models is due to the inward boundary treatment.

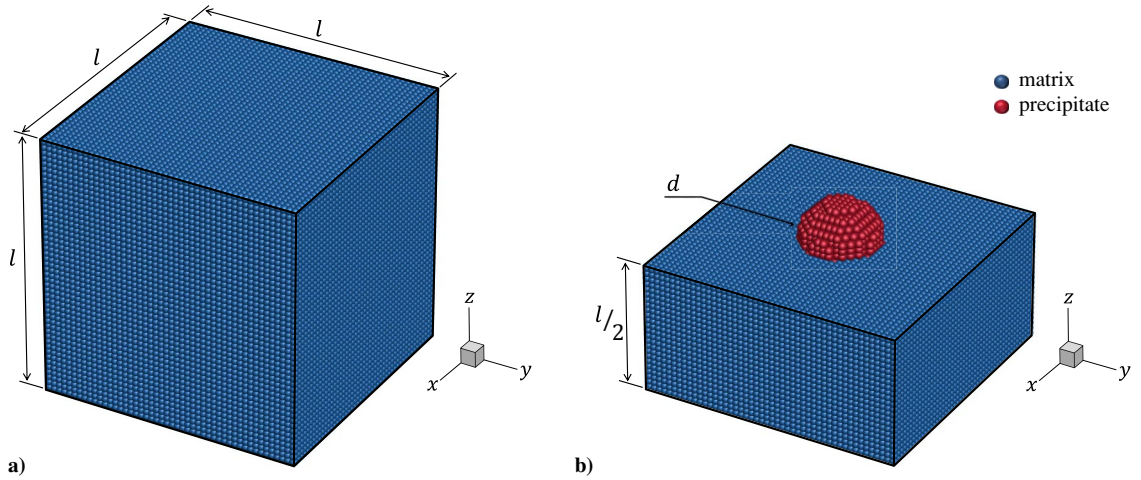

Fig. 15 Three-dimensional matrix with soft precipitate. a) A 3D matrix microstructure (colored in blue) with dimension $l = 3$ mm consisting of a soft precipitate (colored in red) with diameter $d = 0.8750$ mm locating at the center. The material domain is discretized into $48 \times 48 \times 48$ particles with a constant interparticle spacing $h = 62.5$ μm. b) This illustration provides the interior information along the slice $z = 1.5$ mm. The spherical precipitate is fully retained for a better visualization.

$\delta = h$, $2h$, $3h$, and weighting value coefficients without any stabilization framework for $\delta = 2h$, $3h$ [52]. An inward boundary treatment, as outlined in Sec. II.C, is then enforced to constrain the velocity gradients of the shadow particles in PD models. Figure 16 depicts the variations in y-displacement contours at the midsection $z = 1.5$ mm for stabilized PD framework using horizon sizes of $\delta = h$, $2h$, and $3h$ at the final strain value 0.02. FEM simulation prediction is also included for comparison. Although the overall displacement fields are mostly similar between PD and FE models, the localizations around the precipitate as obtained from FEM simulation are comparatively more diffuse due to the lack of an internal length scale.

Next, Fig. 17 depicts the variations in the x-displacement contours for PD technique with and without the stabilization control of zero-energy modes, across the midsection $z = 1.5$ mm using horizon sizes $\delta = 2h$ and $3h$ at the final strain value 0.02. For the case of a PD scheme without any control of zero-energy modes (termed "no control"), an influence function of the form $\omega = 1/\|\boldsymbol{\xi}\|_2$ is employed [52], where $\boldsymbol{\xi}$ denotes the bond vector associated with neighboring material particles. While "no control" simulations tend to produce significant increases in erroneous zero-energy modes with successive horizon sizes, the resultant displacements with higher-order approximation scheme (termed "higher-order") illustrates stabilized solutions for both horizon sizes $\delta = 2h$ and $3h$. Figure 18 depicts the

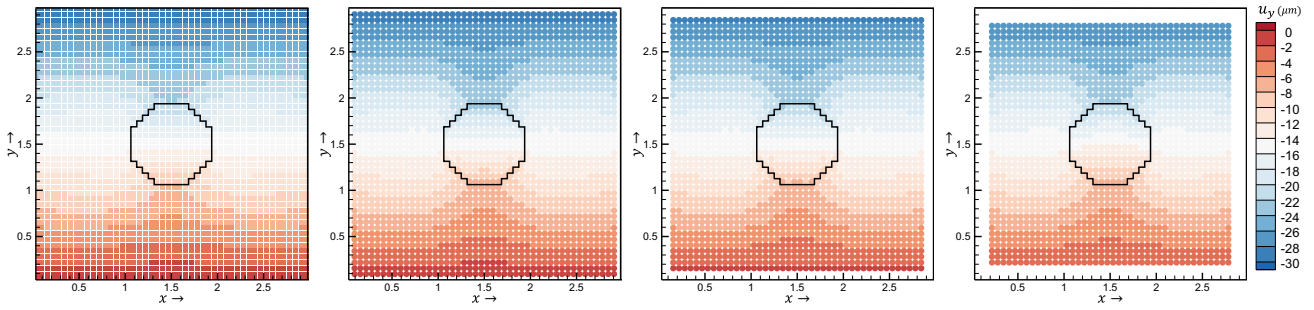

Fig. 16 Comparison of y displacements (in micrometers) between FE and PD techniques with $\delta = h$, $2h$, and $3h$ along midsection at $z = 1.5$ mm at final strain.

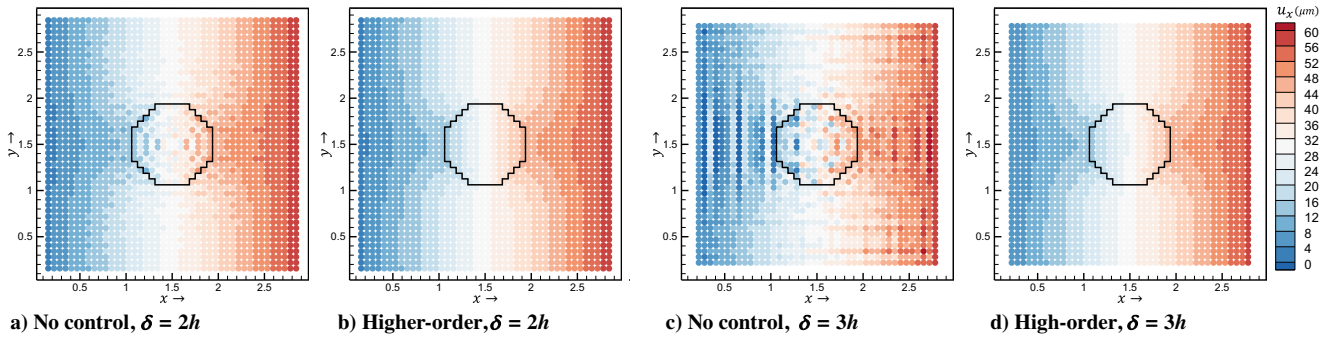

Fig. 17 Contours of x displacements (in micrometers) obtained from PD models with no control of zero-energy modes against proposed higher-order stabilization approach with $\delta = 2h$ and $3h$ along midsection at $z = 1.5$ mm at final strain.

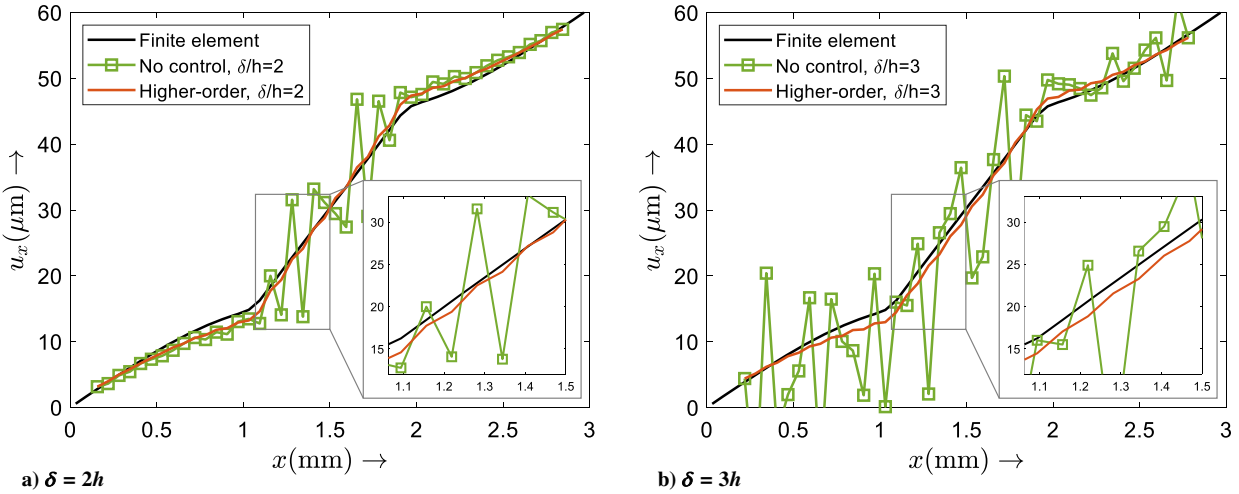

Fig. 18 Contours of x displacements through centerline along the x direction for two horizon interactions a) $\delta = 2h$ and b) $\delta = 3h$, respectively, at final strain.

profiles of x displacements through centerline along the x direction for the contours shown in Fig. 17. The plots here are also compared against the FEM solution as seen in Fig. 16a. Figure 18a exhibits the emergence of the instability modes for the "no control" case of $\delta = 2h$ right across the interface of soft precipitate and stiff matrix, as the hourglass oscillations grow dramatically within the spherical precipitate. In the case of $\delta = 3h$ shown in Fig. 18b, the hourglass oscillations significantly worsen for "no control" procedure, affecting the displacements even along the stiff matrix. In both horizon sizes, the resulting contours pertaining to the higher-order approximation scheme effectively dampen the hourglass oscillations and remain close to the FEM solution.

Thereafter, four additional stiffness constants are assigned to the spherical precipitate using the following ratios: $r_c = 10^{-2}$, 10^{-3}, 10^{-4}, and 10^{-5}, where $C_{ij}^{ppt} = r_c \times C_{ij}^{\text{mat}}$. As the stiffness ratio decreases, the precipitate properties tend toward the properties of a void with a zero modulus. As observed in the previous examples, the interface between a stiff and soft material has particularly sharp gradients in the strain and stress fields. Hence, a non-local theory becomes advantageous due to its ability in capturing discontinuities without enforcing any traction boundary conditions around the precipitate interface. Figure 19 illustrates x- and z-component displacements along the midsection $z = 1.5$ mm as obtained from the stabilized non-local PD simulation using the horizon size $\delta = 3h$ for all the stiffness ratios considered. As the stiffness of the precipitate decreases towards that of a void, one would expect a decreased force transmission across the precipitate interface and, consequently, a decreased displacement at the void's center. As demonstrated in Fig. 19, the stabilized higher-order PD model correctly captures the zero displacements at the center as the elastic modulus pertaining to the spherical precipitate decreases.

Figure 20 denotes the plots for componentwise displacements at the center of the precipitate as a function of the stiffness ratio r_c, for different horizon sizes δ. Here, the FEM predicts close to a constant nonzero displacement at the center. However, one would expect

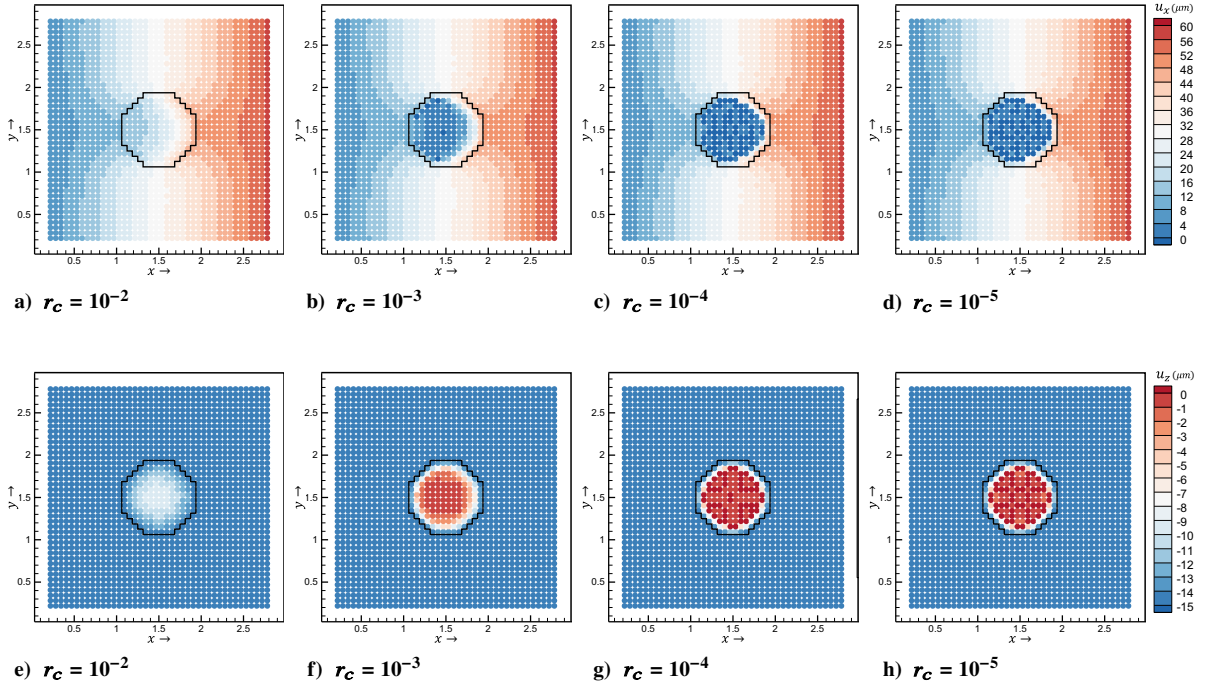

Fig. 19 Comparison of a–d) x displacements and e–h) z displacements (both in micrometers) along midsection $z = 1.5$ mm for varying stiffness ratios as obtained from the high-order stabilized PD model with $\delta = 3h$.

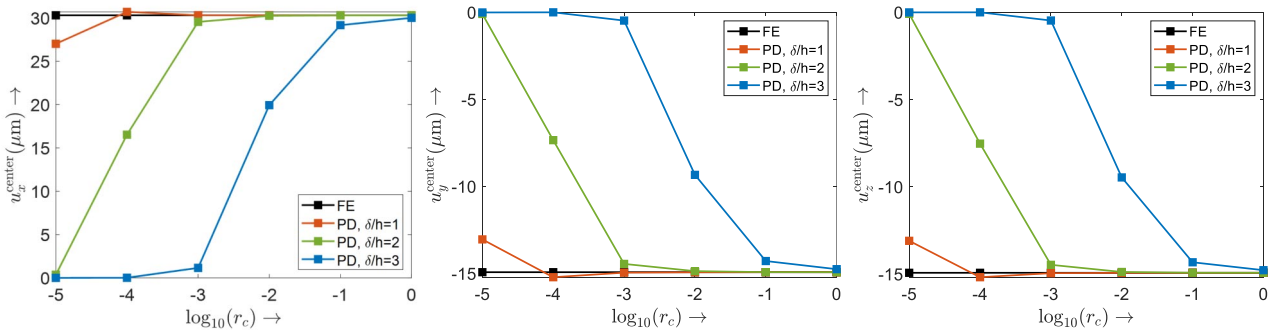

Fig. 20 Variations in the displacement components at the center of the spherical precipitate in terms of the stiffness ratio r_c, for different horizon sizes δ.

convergence toward a zero-displacement because no force transmission occurs across the precipitate interface in the case of a zero-modulus material, e.g., vacuum. Despite that, PD, a non-local method, depicts a faster convergence toward a zero center displacement with growing horizon sizes δ, as the stiffness ratio r_c decreases. For a given horizon size δ, the absolute value of all the displacement components decreases with reducing stiffness ratio r_c. The convergence rate of the non-local PD solutions to the zero displacement at the center of the precipitate depends on the horizon size δ. This is expected as the non-local horizons utilize the information from both sides (i.e., low and high stiffness particles) to capture the sharp strain gradient. Additionally, with a given stiffness ratio r_c, the absolute values of the displacement components drop with increasing horizon size δ. As the horizon size δ increases, the sharp gradient around the void's interface is captured more efficiently because there are more particles to decide upon the interface behavior.

D. Three-Dimensional Polycrystalline Microstructure with Spherical Void

The previous 3D example demonstrates the efficacy of the higher-order stabilization scheme in the case of an elastic matrix. Here, the example includes an elastoplastic 3D model of the polycrystalline aggregates using a soft precipitate with a stiffness ratio $r_c = 0.1$. Specifically, a 3D polycrystalline microstructure consisting of 78 grains with dimensions $l = 3$ mm, and a soft precipitate with diameter $d = 0.8750$ mm at the center is considered. The 3D material domain is discretized into $48 \times 48 \times 48$ particles with a constant interparticle spacing $h = 62.5$ μm as shown in Fig. 21a. Moreover, Fig. 21b illustrates the interior cross section of the 3D polycrystalline microstructure along slice $z = 1.5$ mm without depicting the precipitate region. The polycrystal is simulated with properties of WE43 alloy-T5 temper, as provided by Lakshmanan et al. [18] with 18 slip systems, including 3 basal $\langle a \rangle$, 3 prismatic $\langle a \rangle$, 6 pyramidal $\langle a \rangle$, and 6 pyramidal $\langle c + a \rangle$ slip systems. The boundary conditions are the same as those considered in Sec. III.C.

Figure 22 depicts the x and y strains, with and without control of zero-energy modes, along the midsection $z = 1.5$ mm using a horizon size $\delta = 3h$. For the case of the PD scheme without any control of zero-energy modes (termed "no control"), an influence function $\omega = 1/\|\boldsymbol{\xi}\|_2$ is employed [52] similar to the previous example in Sec. III.C. The no control case shows patchy/pixellated locations not just along the precipitate interface (similar to the elastic matrix example) but also within the grains, where one can expect strain localizations across grain boundaries due to property variations as a function of crystal orientations (i.e., across hard and soft grains depending on their crystal orientations relative to the loading direction). Nevertheless, the results associated with the higher-order stabilization scheme (termed "higher-order") show an effective control of the erroneous zero-energy mode oscillations.

Next, the PD results are compared against the FEM solution in Fig. 23, which depicts the profile of equivalent strain at midsection $z = 1.5$ mm for horizon sizes $\delta = h$, $2h$, and $3h$. Unlike the 3D composite microstructure in Sec. III.C, where there exist significant strain localizations only around the interface of the precipitate; here, there are expected to be strain concentrations across the granular interfaces as well. In the FEM solution, the interfacial

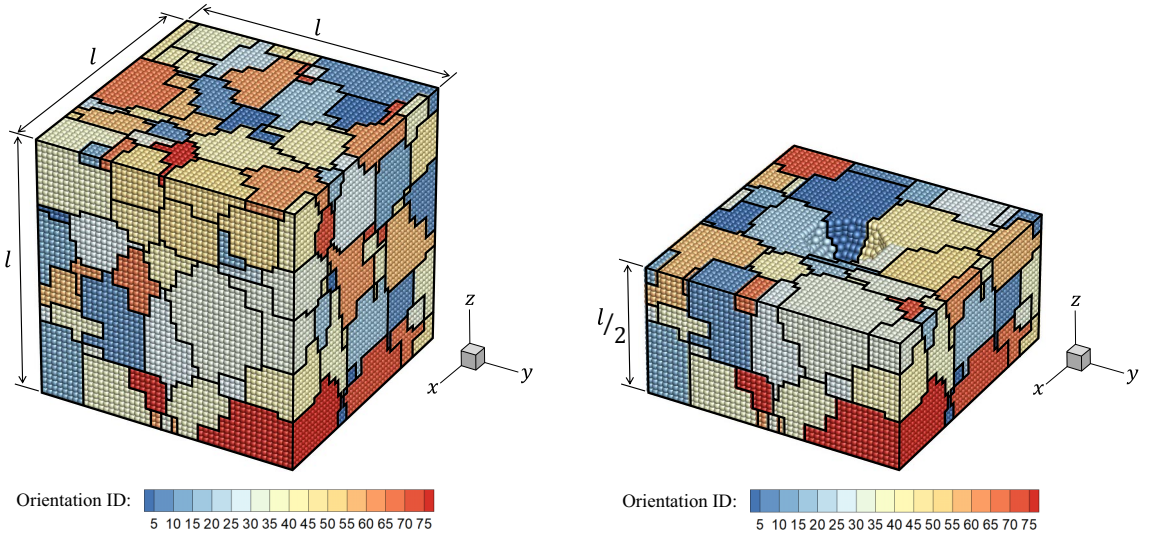

Fig. 21 Three-dimensional polycrystalline microstructure with spherical void. a) A 3D polycrystalline microstructure consisting of 78 grains with dimensions $l = 3$ mm and a soft precipitate with diameter $d = 0.8750$ mm at the center. b) Interior of the 3D microstructure along slice $z = 1.5$ mm. The spherical precipitate at the center is removed for a better visualization. Grains with similar orientation ID share the same Rodrigues orientation vector. The black lines denote grain boundaries.

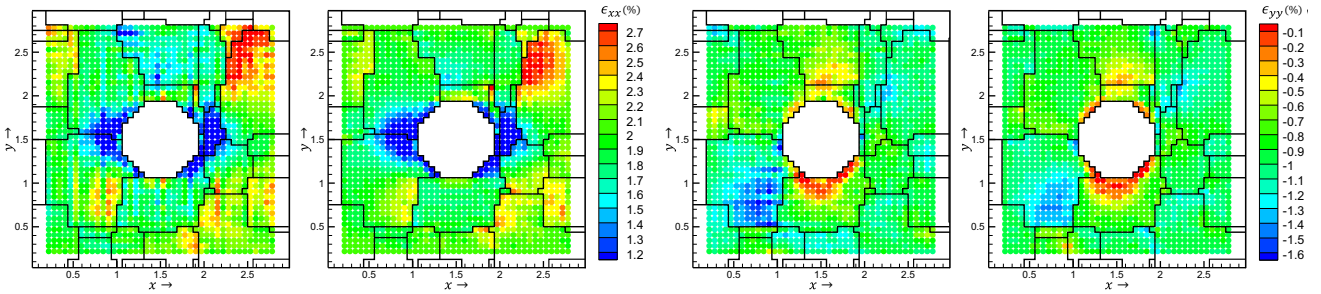

a) No control, ϵ_{xx} b) High-order, ϵ_{xx} c) No control, ϵ_{yy} d) High-order, ϵ_{yy}

Fig. 22 Contours of a,b) ϵ_{xx} and c,d) ϵ_{yy} (in %) obtained from PD models with no control of zero-energy modes against proposed higher-order stabilization approach with $\delta = 3h$ along midsection at $z = 1.5$ mm at final strain value.

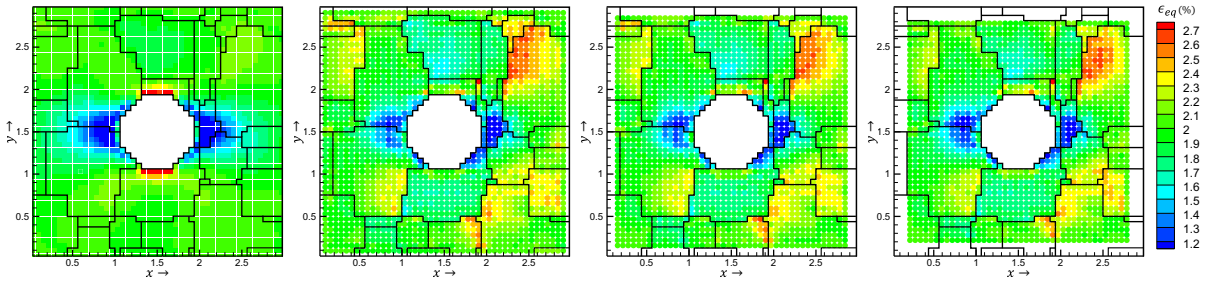

a) FE b) PD, $\delta = h$ c) PD, $\delta = 2h$ d) PD, $\delta = 3h$

Fig. 23 Comparison of equivalent strain (denoted as ϵ_{eq}) (in %) between FE and PD techniques with $\delta = h$, $2h$, and $3h$ along the midsection at $z = 1.5$ mm at final strain.

strain localizations are computed to be significantly more pronounced than the granular strain localizations within each crystal. Contrastingly, the PD solution identifies both strain localizations along the precipitate boundary as well as granular interfaces. Additionally, the PD results are stable across the three horizon sizes $\delta = h, 2h$, and $3h$. Implementation of the higher-order stabilization control in these examples required no additional computational cost per time step, as the influence function values are explicitly adjusted for each user-defined horizon interaction δ. However, as shown by Silling and Askari [53], the maximum stable time step for PD is, in general, also a function of the horizon radius for long-range interactions (i.e., $\delta > h$) and needs to be scaled based on the von Neumann stability analysis as the horizon radius δ rises [41].

IV. Conclusions

In this paper, a higher-order approximation to the non-local deformation gradient is developed to suppress zero-energy instability modes in PD models beyond nearest-neighbor interactions. In microstructural simulations, pixel- or voxel-based structured discretizations are often preferred as they can be readily obtained directly from microscopy, tomographic imaging, or numerical acquisition techniques. As a result, a mesh-less non-ordinary state-based implementation of the PD via Newmark's dynamic method with artificial damping is employed for solving deformation and stress fields on structured grids. However, such correspondence-based PD models often suffer from zero-energy mode oscillations, which, as studied in this paper, can be effectively mitigated by choosing material weight functions via a Taylor series expansion of the deformation gradient. The novelty here is a tensor-based derivation of the linear constraint equations, which can be used to systematically identify the particle interaction weight functions for various user-specified horizon radii. It is demonstrated that unique weighting value coefficients can be obtained by combining the governing equations for the desired leading truncation error, along with additional set of constraint equations from the next higher-order approximations that do not contain first-order interaction weight functions.

The efficacy of the higher-order stabilization method is first demonstrated for a simple 1D elastic cantilever bar, where results are compared with exact and PD solutions with no stabilization control. The zero-energy modes are demonstrated to be effectively dampened using the proposed higher-order particle interaction weight functions. Next, in the case of 2D polycrystalline microstructures, observed shear bands are shown to be stable across different horizon sizes while being relatively sharper and more localized within intergranular regions relative to the FEM solution. The proposed higher-order stabilization scheme is also demonstrated for examples involving 3D composite and polycrystalline microstructures, along with comparisons against FE technique. In addition to the stabilization scheme effectively suppressing the zero-energy mode oscillations, it is shown that the PD approach, unlike FEM, converges toward a zero displacement in the precipitate with a decrease in the stiffness. Overall, the presented stabilization scheme can lead to high-quality and consistent non-ordinary state-based results for PD simulations beyond nearest-neighbor interactions. Furthermore, the proposed higher-order approximation framework can be directly applied to PD problems involving discontinuities such as damage/fracture propagation, once an appropriate damage continuum model is adopted. All the codes and examples constituting the current CPPD implementation will be available in an open-source platform to the community upon publication of the work.

Appendix: Adaptive Dynamic Relaxation Scheme

In the absence of body forces, the equation of motion as shown in Eq. (3) can be rewritten in a vector form as follows:

$$\ddot{\boldsymbol{u}}(\boldsymbol{x}, t) + c\dot{\boldsymbol{u}}(\boldsymbol{x}, t) = \boldsymbol{f}(\boldsymbol{u}, \boldsymbol{x}, t) \tag{A1}$$

where c is a damping coefficient, and the force vector $\boldsymbol{f}$ is defined as $\boldsymbol{f}(\boldsymbol{u}, \boldsymbol{x}, t) = \boldsymbol{\Lambda}^{-1}\boldsymbol{L}(\boldsymbol{x}, t)$, in which $\boldsymbol{\Lambda}$ is a diagonal fictitious density matrix. Based on the adaptive dynamic relaxation method, the most desired density matrix and damping coefficient can be determined

using Greschgorin's theorem and Rayleigh's quotient, respectively [61].

Let $\boldsymbol{u}^n$, $\dot{\boldsymbol{u}}^n$, $\ddot{\boldsymbol{u}}^n$, and $\boldsymbol{f}^n$ denote the displacement, velocity, acceleration, and force vector fields for a given material particle at $t = t_n$, respectively. In the central difference scheme, the velocity and acceleration vectors can be approximated as follows:

$$\dot{\boldsymbol{u}}^n \approx \frac{\boldsymbol{u}^{n+1} - \boldsymbol{u}^{n-1}}{2\Delta t} \tag{A2}$$

$$\ddot{\boldsymbol{u}}^n \approx \frac{\boldsymbol{u}^{n+1} - 2\boldsymbol{u}^n + \boldsymbol{u}^{n-1}}{\Delta t^2} \tag{A3}$$

where Δt refers to the incremental time step. Substituting Eqs. (A2) and (A3) into Eq. (A1) while rearranging the terms yields an updated scheme for the displacement field:

$$\boldsymbol{u}^{n+1} = \frac{2\Delta t^2 \boldsymbol{f}^n + 4\boldsymbol{u}^n + (c\Delta t - 2)\boldsymbol{u}^{n-1}}{2 + c\Delta t} \tag{A4}$$

Accordingly, Eq. (A5) is employed to estimate $\boldsymbol{u}^{-1}$ for initialization of the displacement update:

$$\boldsymbol{u}^{-1} = \boldsymbol{u}^0 - \Delta t\dot{\boldsymbol{u}}^0 + \frac{\Delta t^2}{2}\ddot{\boldsymbol{u}}^0 \tag{A5}$$

where $\boldsymbol{u}^0$, $\dot{\boldsymbol{u}}^0$, and $\ddot{\boldsymbol{u}}^0$ are the initial displacement, velocity, and acceleration vectors, respectively. The velocity and acceleration vectors may subsequently be updated using Eqs. (A2) and (A3). With the assumption of a unit diagonal matrix $\boldsymbol{\Lambda}$, the time step Δt can be selected based on Greschgorin's theorem [61], as expressed in the following:

$$\Delta t \leq \sqrt{\frac{4\Lambda_{ii}}{\sum_j |K_{ij}|}} = \sqrt{\frac{4}{\sum_j |K_{ij}|}} = \sqrt{\frac{4}{\|\boldsymbol{K}\|_\infty}} \tag{A6}$$

where Λ_{ii} represents the diagonal coefficients of the density matrix, $\boldsymbol{K}$ denotes the stiffness matrix of the system, and $\|\cdot\|_\infty$ denotes the vector-induced matrix ∞ norm. Because the stiffness matrix K_{ij} is not explicitly computed, another approximation scheme can be applied for the computation of time step size. An appropriate value of Δt for the 1D PD model is based on the wave speed, denoted as c_s, using the Courant–Friedrichs–Lewy (CFL) condition [54]:

$$\Delta t \leq \frac{2\Delta x}{c_s} \tag{A7}$$

where Δx represents the minimal grid size, or the minimal bond length in PD modeling. In higher-dimensional problems, however, the CFL condition becomes stringent. For an n-dimensional problem with a uniform grid, the critical Δt may be estimated as:

$$\Delta t \leq \frac{2\Delta x}{n}\sqrt{\frac{\rho}{E_{\max}}} \tag{A8}$$

where $E_{\max}$ is the largest eigenvalue of the elastic stiffness matrix. It is worth noting that the CFL condition in Eq. (A8) can be conservative because the derivation is based solely on the nearest neighbors [53].

Next, the damping ratio c is selected based on the lowest frequency of the system using Rayleigh's quotient [61]:

$$c^n = 2\sqrt{\frac{(\boldsymbol{u}^n)^T \boldsymbol{k}^n \boldsymbol{u}^n}{(\boldsymbol{u}^n)^T \boldsymbol{u}^n}} \tag{A9}$$

where $\boldsymbol{k}^n$ is a diagonal local stiffness matrix given by:

$$k_{ii}^n = -\frac{1}{\Lambda_{ii}}\frac{f_i^n - f_i^{n-1}}{u_i^n - u_i^{n-1}} = -\frac{f_i^n - f_i^{n-1}}{u_i^n - u_i^{n-1}} \tag{A10}$$

Here, f_i^n is the ith component of the force vector $\boldsymbol{f}$, at time $t = t_n$. Because the local stiffness matrix calculation involves division by the difference of displacements in consecutive time steps, it is plausible to encounter a division by zero. Accordingly, the local stiffness k_{ii}^n is set to zero, when the difference between displacement fields vanishes. Finally, a guess damping ratio c_0 can be chosen to start the computation.

Data Availability

The executable files, as well as raw/processed data required to reproduce the findings in this paper, are available upon request.

Acknowledgments

The authors would like to acknowledge the Air Force Office of Scientific Research (AFOSR), Materials for Extreme Environments Program (Grant No. FA9550-18-1-0091), as well as the National Science Foundation (NSF) Graduate Research Fellowship Program (Grant No. DGE 1841052) for financial support. The computations in this paper have been carried out as part of research supported by the U.S. Department of Energy (DoE), Office of Basic Energy Sciences, Division of Materials Sciences and Engineering (Grant No. DE-SC0008637), which funds the PRedictive Integrated Structural Materials Science (PRISMS) Center at the University of Michigan. The authors wish to thank John A. Newman and Stephen W. Smith at the Durability, Damage Tolerance, and Reliability (DDTR) Branch in NASA Langley Research Center for providing valuable discussion, support, and motivation for this paper.

References

[1] Sun, S., and Sundararaghavan, V., "A Peridynamic Implementation of Crystal Plasticity," *International Journal of Solids and Structures*, Vol. 51, Nos. 19–20, 2014, pp. 3350–3360. https://doi.org/10.1016/j.ijsolstr.2014.05.027

[2] Roters, F., Eisenlohr, P., Hantcherli, L., Tjahjanto, D. D., Bieler, T. R., and Raabe, D., "Overview of Constitutive Laws, Kinematics, Homogenization and Multiscale Methods in Crystal Plasticity Finite-Element Modeling: Theory, Experiments, Applications," *Acta Materialia*, Vol. 58, No. 4, 2010, pp. 1152–1211. https://doi.org/10.1016/j.actamat.2009.10.058

[3] Ganesan, S., Javaheri, I., and Sundararaghavan, V., "Constrained Voronoi Models for Interpreting Surface Microstructural Measurements," *Mechanics of Materials*, Vol. 159, Aug. 2021, Paper 103892. https://doi.org/10.1016/j.mechmat.2021.103892

[4] Harren, S. V., and Asaro, R. J., "Nonuniform Deformations in Polycrystals and Aspects of the Validity of the Taylor Model," *Journal of the Mechanics and Physics of Solids*, Vol. 37, No. 2, 1989, pp. 191–232. https://doi.org/10.1016/0022-5096(89)90010-0

[5] Beaudoin, A. J., Mecking, H., and Kocks, U. F., "Development of Localized Orientation Gradients in FCC Polycrystals," *Philosophical Magazine A*, Vol. 73, No. 6, 1996, pp. 1503–1517. https://doi.org/10.1080/01418619608242998

[6] Becker, R., and Panchanadeeswaran, S., "Effects of Grain Interactions on Deformation and Local Texture in Polycrystals," *Acta Metallurgica et Materialia*, Vol. 43, No. 7, 1995, pp. 2701–2719. https://doi.org/10.1016/0956-7151(94)00460-Y

[7] Bronkhorst, C. A., Kalidindi, S. R., and Anand, L., "Polycrystalline Plasticity and the Evolution of Crystallographic Texture in FCC Metals," *Philosophical Transactions of the Royal Society of London. Series A: Physical and Engineering Sciences*, Vol. 341, No. 1662, 1992, pp. 443–477. https://doi.org/10.1098/rsta.1992.0111

[8] Inoue, H., and Takasugi, T., "Texture Control for Improving Deep Drawability in Rolled and Annealed Aluminum Alloy Sheets," *Materials Transactions*, Vol. 48, No. 8, 2007, pp. 2014–2022. https://doi.org/10.2320/matertrans.L-MRA2007871

[9] Engler, O., and Hirsch, J., "Texture Control by Thermomechanical Processing of AA6*xxx* Al–Mg–Si Sheet Alloys for Automotive Applications—A Review," *Materials Science and Engineering: A*, Vol. 336,

Nos. 1–2, 2002, pp. 249–262.
https://doi.org/10.1016/S0921-5093(01)01968-2
[10] Sundararaghavan, V., and Zabaras, N., "A Multi-Length Scale Sensitivity Analysis for the Control of Texture-Dependent Properties in Deformation Processing," *International Journal of Plasticity*, Vol. 24, No. 9, 2008, pp. 1581–1605.
https://doi.org/10.1016/j.ijplas.2007.12.005
[11] Summers, E. M., Meloy, R., and Na, S. M., "Magnetostriction and Texture Relationships in Annealed Galfenol Alloys," *Journal of Applied Physics*, Vol. 105, No. 7, 2009, Paper 07A922.
https://doi.org/10.1063/1.3067849
[12] Liu, R., Kumar, A., Chen, A., Agrawal, A., Sundararaghavan, V., and Choudhary, A., "A Predictive Machine Learning Approach for Microstructure Optimization and Materials Design," *Scientific Reports*, Vol. 5, June 2015, paper 11551.
https://doi.org/10.1038/srep11551
[13] Acar, P., and Sundararaghavan, V., "Linear Solution Scheme for Microstructure Design with Process Constraints," *AIAA Journal*, Vol. 54, No. 12, 2016, pp. 4022–4031.
https://doi.org/10.2514/1.J055247
[14] Anand, L., and Kothari, M., "A Computational Procedure for Rate-Independent Crystal Plasticity," *Journal of the Mechanics and Physics of Solids*, Vol. 44, No. 4, 1996, pp. 525–558.
https://doi.org/10.1016/0022-5096(96)00001-4
[15] Calcagnotto, M., Ponge, D., Demir, E., and Raabe, D., "Orientation Gradients and Geometrically Necessary Dislocations in Ultrafine Grained Dual-Phase Steels Studied by 2D and 3D EBSD," *Materials Science and Engineering: A*, Vol. 527, Nos. 10–11, 2010, pp. 2738–2746.
https://doi.org/10.1016/j.msea.2010.01.004
[16] Ruggles, T. J., and Fullwood, D. T., "Estimations of Bulk Geometrically Necessary Dislocation Density Using High Resolution EBSD," *Ultramicroscopy*, Vol. 133, 2013, pp. 8–15.
https://doi.org/10.1016/j.ultramic.2013.04.011
[17] Armero, F., and Garikipati, K., "An Analysis of Strong Discontinuities in Multiplicative Finite Strain Plasticity and Their Relation with the Numerical Simulation of Strain Localization in Solids," *International Journal of Solids and Structures*, Vol. 33, Nos. 20–22, 1996, pp. 2863–2885.
https://doi.org/10.1016/0020-7683(95)00257-X
[18] Lakshmanan, A., Luo, J., Javaheri, I., and Sundararaghavan, V., "Three-Dimensional Crystal Plasticity Simulations Using Peridynamics Theory and Experimental Comparison," *International Journal of Plasticity*, Vol. 142, July 2021, Paper 102991.
https://doi.org/10.1016/j.ijplas.2021.102991
[19] Silling, S. A., "Reformulation of Elasticity Theory for Discontinuities and Long-Range Forces," *Journal of the Mechanics and Physics of Solids*, Vol. 48, No. 1, 2000, pp. 175–209.
https://doi.org/10.1016/S0022-5096(99)00029-0
[20] Warren, T. L., Silling, S. A., Askari, A., Weckner, O., Epton, M. A., and Xu, J., "A Non-Ordinary State-Based Peridynamic Method to Model Solid Material Deformation and Fracture," *International Journal of Solids and Structures*, Vol. 46, No. 5, 2009, pp. 1186–1195.
https://doi.org/10.1016/j.ijsolstr.2008.10.029
[21] Madenci, E., and Oterkus, E., *Peridynamic Theory and Its Applications*, Springer, Berlin, 2014, pp. 19–43.
https://doi.org/10.1007/978-1-4614-8465-3_2
[22] Gerstle, W. H., *Introduction to Practical Peridynamics: Computational Solid Mechanics Without Stress and Strain*, Vol. 1, World Scientific Publ., Singapore, 2015, pp. 146–173.
https://doi.org/10.1142/9789814699556_0005
[23] Tupek, M. R., and Radovitzky, R., "An Extended Constitutive Correspondence Formulation of Peridynamics Based on Nonlinear Bond-Strain Measures," *Journal of the Mechanics and Physics of Solids*, Vol. 65, April 2014, pp. 82–92.
https://doi.org/10.1016/j.jmps.2013.12.012
[24] Butt, S. N., and Meschke, G., "Peridynamic Analysis of Dynamic Fracture: Influence of Peridynamic Horizon, Dimensionality and Specimen Size," *Computational Mechanics*, Vol. 67, No. 6, 2021, pp. 1719–1745.
https://doi.org/10.1007/s00466-021-02017-1
[25] Agwai, A., Guven, I., and Madenci, E., "Predicting Crack Propagation with Peridynamics: a Comparative Study," *International Journal of Fracture*, Vol. 171, No. 1, 2011, pp. 65–78.
https://doi.org/10.1007/s10704-011-9628-4
[26] Gu, X., Zhang, Q., and Madenci, E., "Non-Ordinary State-Based Peridynamic Simulation of Elastoplastic Deformation and Dynamic Cracking of Polycrystal," *Engineering Fracture Mechanics*, Vol. 218, Sept. 2019, Paper 106568.
https://doi.org/10.1016/j.engfracmech.2019.106568
[27] Silling, S. A., Epton, M., Weckner, O., Xu, J., and Askari, E., "Peridynamic States and Constitutive Modeling," *Journal of Elasticity*, Vol. 88, No. 2, 2007, pp. 151–184.
https://doi.org/10.1007/s10659-007-9125-1
[28] Silling, S. A., and Lehoucq, R. B., "Peridynamic Theory of Solid Mechanics," *Advances in Applied Mechanics*, Vol. 44, Elsevier, New York, 2010, pp. 73–168.
https://doi.org/10.1016/S0065-2156(10)44002-8
[29] Yaghoobi, M., Ganesan, S., Sundar, S., Lakshmanan, A., Rudraraju, S., Allison, J. E., and Sundararaghavan, V., "PRISMS-Plasticity: An Open-Source Crystal Plasticity Finite Element Software," *Computational Materials Science*, Vol. 169, Nov. 2019, Paper 109078.
https://doi.org/10.1016/j.commatsci.2019.109078
[30] Yaghoobi, A., and Chorzepa, M. G., "Higher–Order Approximation to Suppress the Zero-Energy Mode in Non-Ordinary State-Based Peridynamics," *Computers and Structures*, Vol. 188, Aug. 2017, pp. 63–79.
https://doi.org/10.1016/j.compstruc.2017.03.019
[31] Tupek, M. R., Rimoli, J. J., and Radovitzky, R., "An Approach for Incorporating Classical Continuum Damage Models in State-Based Peridynamics," *Computer Methods in Applied Mechanics and Engineering*, Vol. 263, Aug. 2013, pp. 20–26.
https://doi.org/10.1016/j.cma.2013.04.012
[32] Ha, Y. D., and Bobaru, F., "Studies of Dynamic Crack Propagation and Crack Branching with Peridynamics," *International Journal of Fracture*, Vol. 162, Nos. 1–2, 2010, pp. 229–244.
https://doi.org/10.1007/s10704-010-9442-4
[33] Silling, S. A., "Stability of Peridynamic Correspondence Material Models and Their Particle Discretizations," *Computer Methods in Applied Mechanics and Engineering*, Vol. 322, Aug. 2017, pp. 42–57.
https://doi.org/10.1016/j.cma.2017.03.043
[34] Li, P., Hao, Z., and Zhen, W., "A Stabilized Non-Ordinary State-Based Peridynamic Model," *Computer Methods in Applied Mechanics and Engineering*, Vol. 339, Sept. 2018, pp. 262–280.
https://doi.org/10.1016/j.cma.2018.05.002
[35] Gu, X., Zhang, Q., Madenci, E., and Xia, X., "Possible Causes of Numerical Oscillations in Non-Ordinary State-Based Peridynamics and a Bond-Associated Higher-Order Stabilized Model," *Computer Methods in Applied Mechanics and Engineering*, Vol. 357, Dec. 2019, Paper 112592.
https://doi.org/10.1016/j.cma.2019.112592
[36] Breitenfeld, M. S., Geubelle, P. H., Weckner, O., and Silling, S. A., "Non-Ordinary State-Based Peridynamic Analysis of Stationary Crack Problems," *Computer Methods in Applied Mechanics and Engineering*, Vol. 272, April 2014, pp. 233–250.
https://doi.org/10.1016/j.cma.2014.01.002
[37] Littlewood, D. J., "A Nonlocal Approach to Modeling Crack Nucleation in AA 7075-T651," *ASME 2011 International Mechanical Engineering Congress and Exposition*, American Soc. of Mechanical Engineers Paper 2011-64236, New York, 2011, pp. 567–576.
https://doi.org/10.1115/IMECE2011-64236
[38] Littlewood, D. J., "Simulation of Dynamic Fracture Using Peridynamics, Finite Element Modeling, and Contact," *ASME International Mechanical Engineering Congress and Exposition*, Vol. 44465, April 2010, pp. 209–217.
https://doi.org/10.1115/IMECE2010-40621
[39] Wan, J., Chen, Z., Chu, X., and Liu, H., "Improved Method for Zero-Energy Mode Suppression in Peridynamic Correspondence Model," *Acta Mechanica Sinica*, Vol. 35, No. 5, 2019, pp. 1021–1032.
https://doi.org/10.1007/s10409-019-00873-y
[40] Wu, C. T., and Ben, B., "A Stabilized Non-Ordinary State-Based Peridynamics for the Nonlocal Ductile Material Failure Analysis in Metal Machining Process," *Computer Methods in Applied Mechanics and Engineering*, Vol. 291, July 2015, pp. 197–215.
https://doi.org/10.1016/j.cma.2015.03.003
[41] Luo, J., and Sundararaghavan, V., "Stress-Point Method for Stabilizing Zero-Energy Modes in Non-Ordinary State-Based Peridynamics," *International Journal of Solids and Structures*, Vol. 150, Oct. 2018, pp. 197–207.
https://doi.org/10.1016/j.ijsolstr.2018.06.015
[42] Cui, H., Li, C., and Zheng, H., "A Higher-Order Stress Point Method for Non-Ordinary State-Based Peridynamics," *Engineering Analysis with Boundary Elements*, Vol. 117, 2020, pp. 104–118.
https://doi.org/10.1016/j.enganabound.2020.03.016
[43] Madenci, E., Barut, A., and Futch, M., "Peridynamic Differential Operator and Its Applications," *Computer Methods in Applied Mechanics and Engineering*, Vol. 304, June 2016, pp. 408–451.
https://doi.org/10.1016/j.cma.2016.02.028
[44] Madenci, E., Dorduncu, M., Barut, A., and Phan, N., "Weak Form of Peridynamics for Nonlocal Essential and Natural Boundary Conditions,"

Computer Methods in Applied Mechanics and Engineering, Vol. 337, Aug. 2018, pp. 598–631.
https://doi.org/10.1016/j.cma.2018.03.038

[45] Rabczuk, T., Ren, H., and Zhuang, X., "A Nonlocal Operator Method for Partial Differential Equations with Application to Electromagnetic Waveguide Problem," *Computers, Materials & Continua*, Vol. 59, No. 1, 2019, p. 2019.
https://doi.org/10.32604/cmc.2019.04567

[46] Madenci, E., Dorduncu, M., Phan, N., and Gu, X., "Weak Form of Bond-Associated Non-Ordinary State-Based Peridynamics Free of Zero Energy Modes with Uniform or Non-Uniform Discretization," *Engineering Fracture Mechanics*, Vol. 218, Sept. 2019, Paper 106613.
https://doi.org/10.1016/j.engfracmech.2019.106613

[47] Chen, H., "Bond-Associated Deformation Gradients for Peridynamic Correspondence Model," *Mechanics Research Communications*, Vol. 90, June 2018, pp. 34–41.
https://doi.org/10.1016/j.mechrescom.2018.04.004

[48] Chen, H., and Spencer, B. W., "Peridynamic Bond-Associated Correspondence Model: Stability and Convergence Properties," *International Journal for Numerical Methods in Engineering*, Vol. 117, No. 6, 2019, pp. 713–727.
https://doi.org/10.1002/nme.5973

[49] Javaheri, I., and Sundararaghavan, V., "Polycrystalline Microstructure Reconstruction Using Markov Random Fields and Histogram Matching," *Computer-Aided Design*, Vol. 120, March 2020, Paper 102806.
https://doi.org/10.1016/j.cad.2019.102806

[50] Javaheri, I., Andani, M. T., and Sundararaghavan, V., "Large-Scale Synthesis of Metal Additively-Manufactured Microstructures Using Markov Random Fields," *Computational Materials Science*, Vol. 206, April 2022, Paper 111228.
https://doi.org/10.1016/j.commatsci.2022.111228

[51] Luo, J., Ramazani, A., and Sundararaghavan, V., "Simulation of Micro–Scale Shear Bands Using Peridynamics with an Adaptive Dynamic Relaxation Method," *International Journal of Solids and Structures*, Vol. 130, Jan. 2018, pp. 36–48.
https://doi.org/10.1016/j.ijsolstr.2017.10.019

[52] Parks, M. L., Seleson, P., Steven, J. P., Silling, S. A., and Lehoucq, R. B., "Peridynamics with LAMMPS: A User Guide, v 0.3 Beta," Sandia National Lab. TR 2011–8253, Albuquerque, NM, 2011.

[53] Silling, S. A., and Askari, E., "A Meshfree Method Based on the Peridynamic Model of Solid Mechanics," *Computers and Structures*, Vol. 83, Nos. 17–18, 2005, pp. 1526–1535.
https://doi.org/10.1016/j.compstruc.2004.11.026

[54] LeVeque, R. J., *Finite Difference Methods for Ordinary and Partial Differential Equations: Steady-State and Time-Dependent Problems*, SIAM, Philadelphia, 2007, Chap. 10.

[55] Flanagan, D. P., and Belytschko, T., "A Uniform Strain Hexahedron and Quadrilateral with Orthogonal Hourglass Control," *International Journal for Numerical Methods in Engineering*, Vol. 17, No. 5, 1981, pp. 679–706.
https://doi.org/10.1002/nme.1620170504

[56] Javaheri, I., Luo, J., Lakshmanan, A., and Sundararaghavan, V., "Higher-Order Approximations for Stabilizing Zero-Energy Modes in Peridynamics Crystal Plasticity Models with Large Horizon Interactions," *AIAA SciTech 2022 Forum*, AIAA Paper 2022-0073, 2022.
https://doi.org/10.2514/6.2022-0073

[57] Macek, R. W., and Silling, S. A., "Peridynamics Via Finite Element Analysis," *Finite Elements in Analysis and Design*, Vol. 43, No. 15, 2007, pp. 1169–1178.
https://doi.org/10.1016/j.finel.2007.08.012

[58] Kammers, A. D., and Daly, S., "Digital Image Correlation Under Scanning Electron Microscopy: Methodology and Validation," *Experimental Mechanics*, Vol. 53, No. 9, 2013, pp. 1743–1761.
https://doi.org/10.1007/s11340-013-9782-x

[59] Guery, A., Hild, F., Latourte, F., and Roux, S., "Slip Activities in Polycrystals Determined by Coupling DIC Measurements with Crystal Plasticity Calculations," *International Journal of Plasticity*, Vol. 81, June 2016, pp. 249–266.
https://doi.org/10.1016/j.ijplas.2016.01.008

[60] Liu, W., Yang, G., and Cai, Y., "Modeling of Failure Mode Switching and Shear Band Propagation Using the Correspondence Framework of Peridynamics," *Computers & Structures*, Vol. 209, Oct. 2018, pp. 150–162.
https://doi.org/10.1016/j.compstruc.2018.08.007

[61] Kilic, B., and Madenci, E., "An Adaptive Dynamic Relaxation Method for Quasi-Static Simulations Using the Peridynamic Theory," *Theoretical and Applied Fracture Mechanics*, Vol. 53, No. 3, 2010, pp. 194–204.
https://doi.org/10.1016/j.tafmec.2010.08.001

W. Yu
Associate Editor